Design and Development of NbTiVZr Porous Alloys for Energy Applications

By

Ayesha Siddique

School of Chemical and Materials Engineering
National University of Sciences and Technology
2023

Design and Development of NbTiVZr Porous Alloys for Energy Applications

Ayesha Siddique

Reg No: 00000320584

This thesis is submitted as a partial fulfillment of the requirements for the degree of

MS in Materials and Surface Engineering

Supervisor Name: Dr. Khurram Yaqoob

School of Chemical and Materials Engineering (SCME)

National University of Sciences and Technology (NUST)
H-12 Islamabad, Pakistan
April, 2023

Dedication

I dedicate this thesis to my parents for their encouragement and support.

Acknowledgements

First and foremost, I would like to thank Allah Almighty for providing me the courage and chance to start this research project and to finish it successfully. This work would not have been possible without His blessings.

I wish to express my sincere gratitude to my supervisor, Dr Khurram Yaqoob, for being such an incredible mentor to me. I would like to thank him for his support, guidance, and assistance during my research, as well as for helping me grow as a research scientist. I'm also grateful for the help from my lab mates and seniors.

Finally, I would like to thank my family and friends for their unwavering support and inspiration. To the ones that matter most in my life, my parents, my siblings, this research work could only be completed with your support.

Ayesha Siddique

Reg No. 00000320584

Abstract

The electrochemical activity and electronic conductivity of multi component metal oxides are at least two orders of magnitude higher than those of single component oxides. Multicomponent porous HEAs are one of the possible candidates in this regard for the supercapacitor electrode. Equiatomic NbTiVZr high entropy alloys with varying concentration of filler element was designed by Thermocalc software and fabricated by arc melting route. As-cast NbTiVZrY HEA consists of two interconnected BCC (Nb, Ti, V, Zr), and Hcp (Y) phases formed by phase separation. 3D foam structure with porosity range (5, 10, 12 and 15 At. %) was obtained by selectively dissolving the Hcp phase in nitric acid solution. When used as an electrode material for supercapacitor, porous high entropy alloy (FS5) exhibits high areal capacitance of 82.66 mF cm^{-2} as compared to its solid counterpart S1 (1.96 mF cm^{-2}) at the scan rate of 2 mV sec^{-1}. At the current density of 1 mA cm^{-2}, the superior capacitance retention value of 104% after 5000 cycles is also attained. Developed samples also have the capability to operate in wide potential window ($\Delta V = 2V$) in 1M Na_2SO_4 solution making them suitable candidate for integration in devices. Subsequently, the prepared high entropy foams have good potential as electrode material for supercapacitor application.

Table of Contents

List of Figures

List of Tables

Chapter:1

Introduction

1.1 Renewable Sources of Energy:

Climate change, rapid population growth and limited resources of fuel and energy have compelled the scientists to explore new energy sources to meet its need [1]. Apprehensions about sustainable energy are encouraging the scientists to develop reliable renewable sources of energy having less negative impact on environment. Technology development for alternative energy sources, in recent specifically on wind, solar and has been hasten. In comparison to non-renewable energy sources like coal etc, the main challenge faced by renewable energy sources is its supply and storage at reasonable price [2].

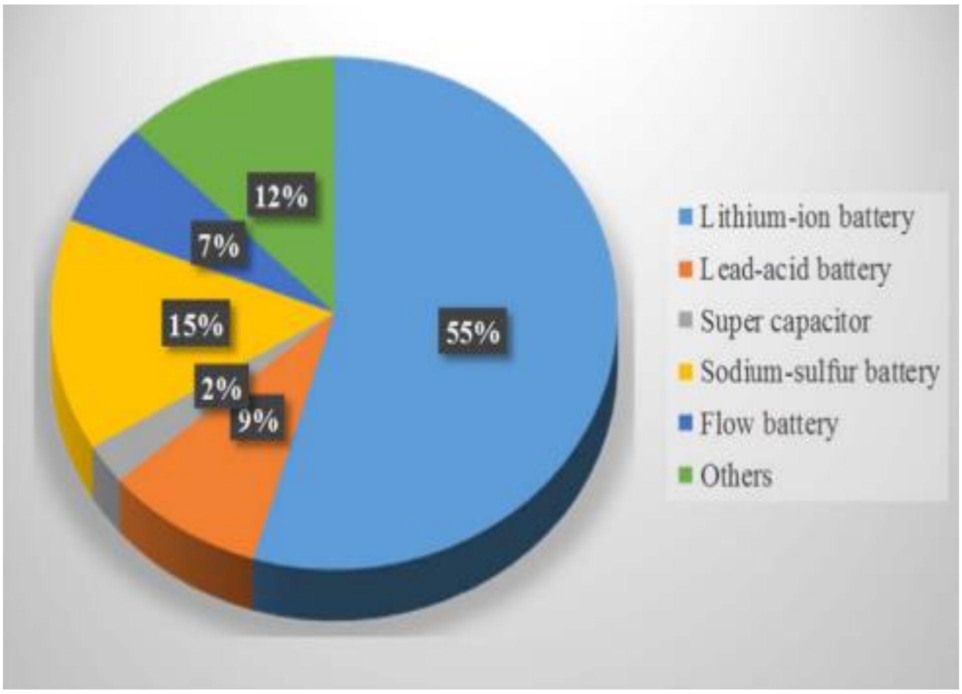

Figure 1: Energy storage system globally.

1.2 Energy Storage Devices:

The formation of environmentally friendly, new and reasonably priced energy storage devices is crucial to meet ecological concerns of modern society. [3]. In this context, supercapacitors, batteries [2], conventional capacitors, fuel cells [1] technologies for energy supply and storage are being developed for energy supply and storage; research is still required to achieve cost competitiveness and greater device efficiency [2]. The most common energy storage devices that come in electrical and electrochemical systems are supercapacitors and batteries [4].

Table 1: Comparison of energy storage devices [4].

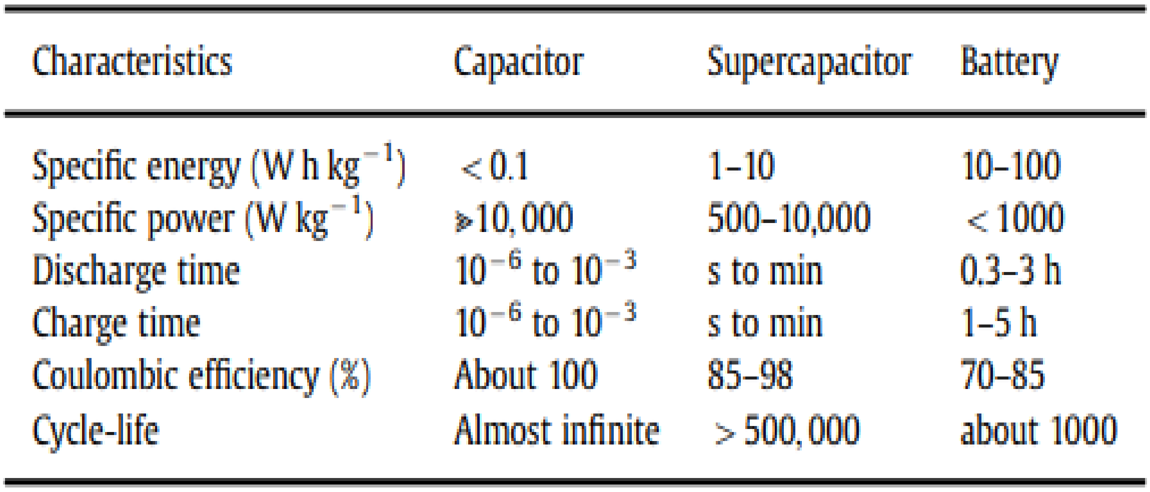

Characteristics	Capacitor	Supercapacitor	Battery
Specific energy (W h kg^{-1})	< 0.1	1–10	10–100
Specific power (W kg^{-1})	$\gg 10{,}000$	500–10,000	< 1000
Discharge time	10^{-6} to 10^{-3}	s to min	0.3–3 h
Charge time	10^{-6} to 10^{-3}	s to min	1–5 h
Coulombic efficiency (%)	About 100	85–98	70–85
Cycle-life	Almost infinite	$> 500{,}000$	about 1000

1.2.1 Batteries and Supercapacitors:

Supercapacitors have not been studied as thoroughly as batteries over the last few years. Though, supercapacitors possess interesting properties, that make them appealing for variety of applications, e.g. in comparison to batteries they can deliver ten times more power. Charging and discharging rate of supercapacitors are high along with their longer cycle life. In some applications, such factors allow supercapacitors, especially redox supercapacitors, to replace or complement batteries. Redox supercapacitors exhibit better properties than conventional batteries due to their charge storage mechanism. [2].

Li-ion batteries non aqueous batteries and Ni-MH aqueous batteries are at present, rechargeable batteries that mainly store charge through massive diffusion or through cations (Li+ or H+) insertion and disinsertion. As a result of insertion/disinsertion and bulk diffusion of cations into the electrode material, it undergoes compositional and phase changes. The diffusion-controlled nature of this process makes it slow and limits the power density i.e. charge-discharge rate [2].

When the electrode material is in the form layers e.g in pseudocapacitive materials cations move in the van der walls gaps. Cations, through charge transfer process can also adsorb electrochemically on surface of electrode material. When they get adsorbed on surface or move into the lattice planes, in both the cases reduction of metal atoms takes place. Adsorption of charges at the surface is fast whereas it movement into interlayer lattice planes is slow phenomena.

In several instances, it has been shown that cations can easily diffuse into the Van der walls gaps, therefore it can be considered as capacitive phenomena, commonly known as intercalation pseudo capacitance. Since there is no change in the composition and phase of electrode material when faradic storage of cations takes place, hence Conway and co-workers call this as process as pseudocapacitive one. The rate of cation storage through pseudocapacitive is fast in comparison to bulk diffusion phenomena [2].

1.2.1.1 Difference between Supercapacitors and Batteries:

The main distinction between batteries and supercapacitors is that several changes occur in the composition as well phase throughout the charge and discharge processes in batteries. It makes the process slow and lowers the power density i.e charge-discharge rate, because it is controlled by diffusion, as batteries mainly store charge through bulk diffusion. Whereas in supercapacitors, storage of cations is fast as they are stored faradaically and there are no changes the electrode material's composition and phases. In contrast to diffusion-controlled processes in batteries, reaction in supercapacitors is kinetically controlled and occurs at a greater pace over the time scale of interest.

Table 2: Comparison of batteries and supercapacitors.

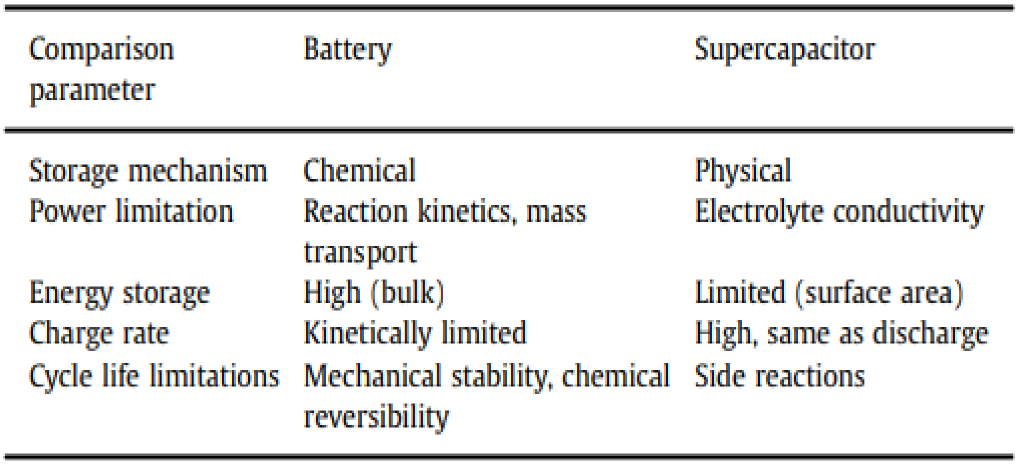

Comparison parameter	Battery	Supercapacitor
Storage mechanism	Chemical	Physical
Power limitation	Reaction kinetics, mass transport	Electrolyte conductivity
Energy storage	High (bulk)	Limited (surface area)
Charge rate	Kinetically limited	High, same as discharge
Cycle life limitations	Mechanical stability, chemical reversibility	Side reactions

The kind of energy storage system to be used depends on the speed of storage process as well as power needed by an application. Applications requiring a higher discharge rate use capacitors, whereas those requiring a slower discharge rate use batteries [3].

1.3 Supercapacitors:

The term super capacitor was introduced by NEC in 1978. The energy storage technology known as electrochemical capacitors (ECs), sometimes known as supercapacitors, is being developed to supplement other storage systems like batteries and to meet the rising energy demands of modern technologies [5]. Because of the presence of longer stability, moderate energy density, fast charge-discharge, [1], long life cycle, high-power density, fast power energy delivery[6] low maintenance and low weight, flexible packaging, wide temperature range (-40 °C to 70 °C), all of these properties make supercapacitors a good device to store energy as compare to old conventional devices that store energy. Ions move from electrolyte toward the surface of electrode material, and this is the basic principal operation of supercapacitors [3].

1.3.1 Classification of Supercapacitors:

Supercapacitors are primarily categorised according to the kind of electrodes they use because their performance is highly dependent on them [7]. As seen in the figure 2 below, SCs can be categorised into three groups, hybrid super-capacitors, pseudocapacitors, and electrical double layer capacitors (EDLCs).

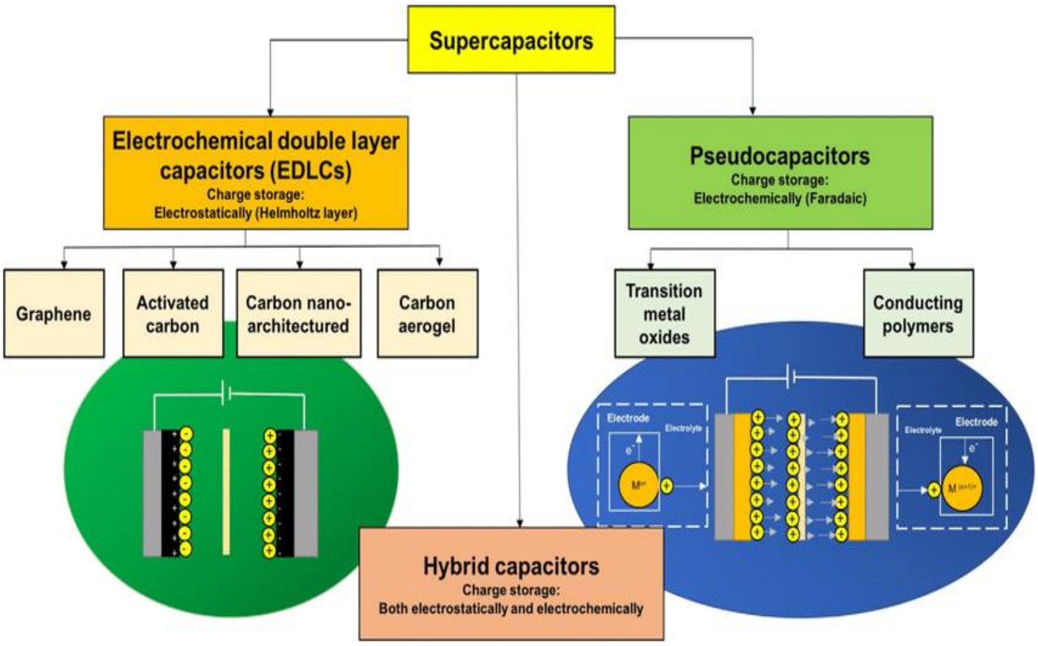

Figure 2: classification of supercapacitors.

1.3.1.1 Electrochemical double layer capacitors (EDLCs):

EDLCs are made up of three main components. First component are the two electrodes that are made up of carbon materials [3] mostly carbon nanotubes and graphene, [8] whereas a separator and electrolyte are second and third components of EDLCs device respectively. In EDLCs charged is not transferred between the electrolyte and electrode material because it is a non-faradic process, rather it is stored electrostatically on the surface of electrode material. There is formation of double layers at the electrodes surface in which energy is stored electrochemically. When the voltage is applied ions moves from electrolyte and after passing through separator they move toward the electrode having opposite charge because attraction between opposite charges occur because of voltage supply. The charges start to accumulate on he surface of electrodes.

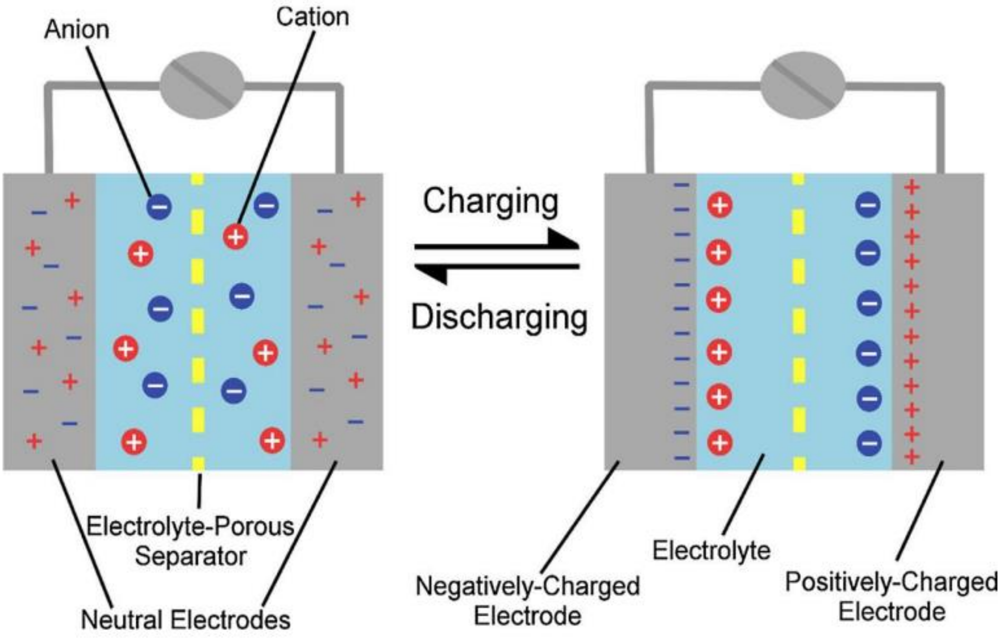

Figure 3: Charge storage mechanism of EDLCs [9].

Moreover, the storage system used by EDLCs enables better power performance, much faster energy uptake and delivery. There is no chemical reaction as a result of the non-faradic process. It prevents the active material's swelling that is seen in batteries during charging and discharging [3]. This benefit allows EDLCs to withstand a high number ($>10^5$) of charge-discharge cycles [7].

According to observations, the capacitance caused by this double layer development ranges from 5 to 20 μF cm^{-2}, depending on the electrolyte used. Moreover, it has been noted that when using acidic or aqueous alkaline electrolytes rather than organic electrolytes in EDLCs, considerably greater specific capacitances are obtained. Hence voltage window obtained in case of EDLCs is small, that causes the energy density to be low as well. As the energy density in capacitors is depends on following factors given below [7]:

$$\boldsymbol{E = \frac{1}{2}CV^2}$$

Hence, EDLCs devices have a low energy density, which lowers their overall performance [2]. To increases the energy density of EDLCs researchers are working on various materials used as electrodes, different electrolytes, temperature ranges in which they can perform [7].

1.3.1.2 Pseudocapacitors:

Conducting polymers and transition metal nitrides are also being studied as electrode materials for pseudocapacitors. Important metal oxides like RuO_2, MnO_2, NiO, TiO_2, SnO_2, CoO, V_2O_5, VO_2, Fe_3O_4, and others are being studied for use in pseudocapacitors [7].

Pseudocapacitors store charge using a faradic mechanism, as opposed to EDLCs, which do it electrostatically. Both the intercalation of charges within the electrode's structure and reversible redox processes at the electrode surface can store charges [7]. In pseudocapacitors when the voltage is applied redox reactions takes places at electrodes and as a result current flow faradaically all through supercapacitors cell. As charges are stored faradaically in case of pseudocapacitors that is why there energy density and specific capacitances are higher than those of EDLCs [3].

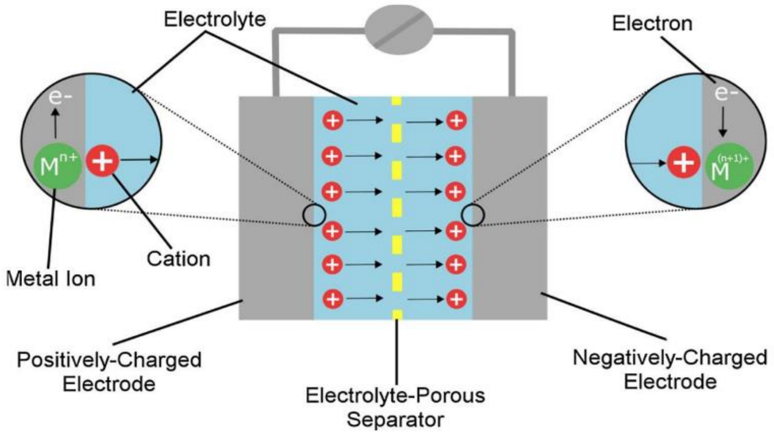

Figure 4: Charge storage mechanism of pseudocapacitors [9].

Even though the specific capacitance of pseudocapacitors is high, but their cyclic stability is low which is their drawback that is caused by the redox processes that occur with each cycle [7], and they also have low power density [3].

1.3.1.3 Hybrid System:

Both EDLCs and Pseudo capacitors have their own pros and cons. Cyclic stability and power performance of EDLCs are high. Whereas the pseudocapacitors have high specific capacitance. Hybrid system make good use of them by having one electrode based on carbon materials which is called as capacitor electrode having high power density whereas the other electrode is made up of metal or polymer-based material i.e battery electrode having good energy density. Hybrid system uses combines both such electrodes in the same cell. By using the correct combination of electrodes, the voltage range of hybrid system can be increased which in turns improves both energy and power densities. Both positive and negative electrodes have been experimented with previously in different combinations, using both aqueous and inorganic electrolytes, yielding varying results.

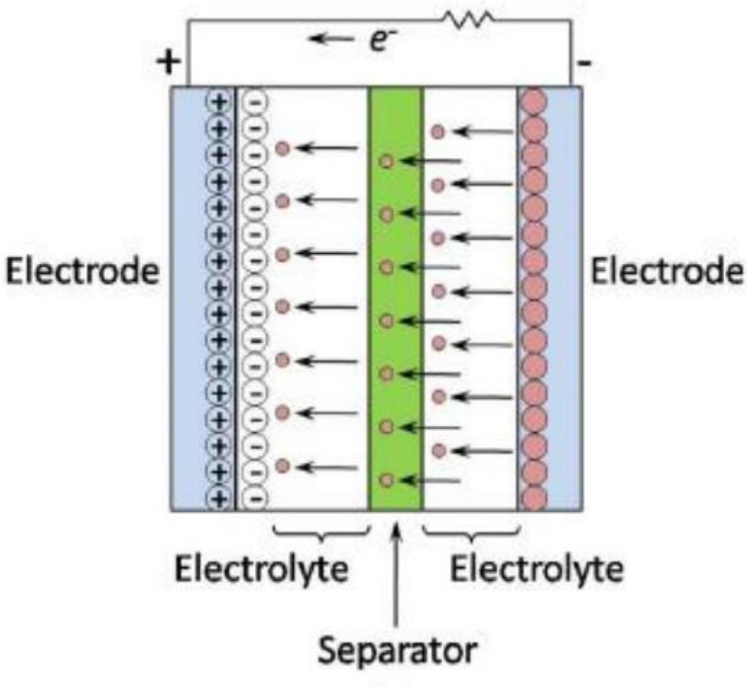

Figure 5: Hybrid Supercapacitor mechanism [10].

When compare with EDLCs, disadvantage faced by hybrid devices is that as one of electrode is battery like that increases the energy density but its cyclic stability is compromised. Thus, while making hybrid devices it is important avoid the formation of regular battery instead of good supercapacitors. Hybrid supercapacitors have three types—Composite, Asymmetric, and Battery-type—that may be identified by their electrode configuration are the current focus of study by researchers [3].

1.3.2 Three electrodes supercapacitor:

Electrodes are made up of different type of materials and type of materials used plays important role on the performance of supercapacitors [7] major focus of this work will be on electrode materials used for supercapacitor applications that will be tested in three electrode setup.

Three electrodes supercapacitor consist of working, counter and reference electrodes and an electrolyte. The electrode material of a super capacitor is its most crucial component [3].

1.3.3 Application of Supercapacitors:

Supercapacitors are useful for applications that need to be very reliable and have a short load cycle, such as electrical cars, load cranes, power quality enhancement, and energy recovery sources like forklifts. Not only in fuel but also in hybrid automobiles supercapacitors can be used. Fuel cells, supercapacitors and batteries can be used all together, and can provide high power capability to store energy from brakes. Because to its large power capacity, a group of supercapacitors can shorten the time it takes for backup power generators to start up during a power outage.

1.3.4 Challenges faced by supercapacitors:

Low capacitance, low energy density, excessive self-discharge, and low voltage per cell are some challenges faced by supercapacitors. Supercapacitors have a larger capacitance than conventional capacitors, although they still have a lower capacitance than batteries and fuel cells. Electrode material can be made up of different novel materials and utilized in supercapacitors to tackle the issue of low capacitance [11]. The choice of electrode material is crucial for supercapacitors since it affects the electrical characteristics [3].

To improve the capacitance, new electrode material for supercapacitors should have high surface area, good conductivity, adjustable pore size[11], pore shape, good surface functionality, permeability of electrolyte solution and wetting of electrode[3]. Designing electroactive materials with better electrochemical characteristics is a major priority. The crucial step is to develop those materials as electrodes that can collect large number electrons and can store large amount of energy. Electrodes of supercapacitors are made up of variety of materials, including metal oxides or hydroxides, conducting polymers, and carbon-based materials [12].

1.3.5 Classification of electrode materials:

The following categories are used to classify electrode materials.

- Carbon materials.
- Polymers based materials.
- Metal oxides

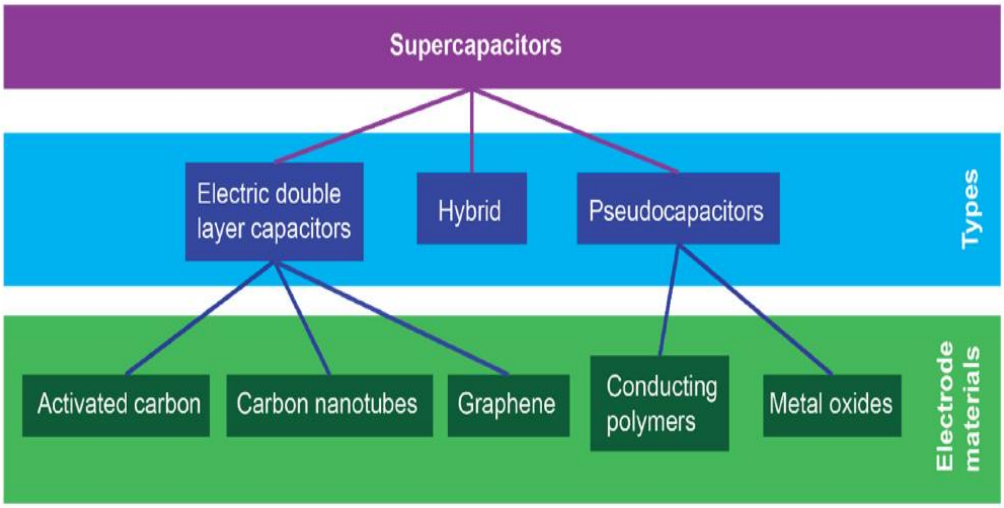

Figure 6: Materials used as electrodes for supercapacitors.

1.3.5.1 Carbon based materials:

Different kind of carbonaceous materials, including carbon nanotubes (CNTs), carbon onions, and carbon derived carbons, have been employed as electrodes for supercapacitors [13]. They provide excellent electrical conductivity, good electrolyte conducting pathways for electrical double layer (EDL) formation and chemical stability [14]. But, carbon-based materials have a limited capacity for charge storage [15].

1.3.5.2 Polymer materials:

The conducting polymer is also striking choice as supercapacitor electrode material [12]. When compared to their counterparts made of metal oxide, they are generally more affordable. In addition to offering greater design flexibility, polymeric electrodes have lower equivalent series resistance. Conducting polymers also have high intrinsic conductivity (1-500 S cm^{-1}) and also have adjustable morphology [7].

The poor rate of charge-discharge caused by the slow speed of ion diffusion within the bulk of these electrode materials is one of their major drawbacks [7]. Polymer based electrode material also show poor electrochemical stability [12].

1.3.5.3 Metal Oxides:

Transition metal oxides (TiO_2, Nb_2O_5, V_2O_5, SnO_2, RuO_2 and FeO) [16] due to their various oxidation states, are potential candidates for supercapacitor applications [17]. In comparison to carbon electrodes, they offer an almost one magnitude larger capacity for energy storage [2]. Because of their low resistance and superior capabilities to store energy due to their capacitance, which comes from the reversible redox reactions on the surface of metal oxides, they make appealing electrode materials, facilitating the production of high-energy and high-power supercapacitors [1].

1.3.6 Issues related with metal oxide electrodes:

- Insufficient surface area
- Low conductivity

The capacitance of metal oxide is lower than hypothetical expectations because of their insufficient surface area and low conductivity [18].

1.3.7 Efforts made to resolve issue related with metal oxide electrodes:

1.3.7.1 Increasing surface area:

1.3.7.1.1 Porous Electrodes:

The large surface-to-volume ratio, high electrical and thermal conductivity, as well as low weight of are distinctive characteristics of porous metallic materials. Porous metal oxide have large surface area [18] as greater deployment of the active material is exhibited, leading to significant increase of capacitance[19]. Porous metal not only provide large intersection for the formation of double layer during charge and discharge in case of EDLCs, they also provide good mechanism for ion movement during redox reaction in case of pseudocapacitors because of their large surface areas. These properties of porous materials can be useful for better performance in supercapacitors[18].

Fast electrolyte ion movement in the bulk and at the surface of electrode is made possible by porous materials. Open porous structure yields satisfactory electrochemical rate performance and high capacitance by ensuring effective contact of electrodes and electrolytes [20].

1.3.7.2 Increasing electronic and Ionic conductivity:

Electronic conductivity can be enhanced by exploring (i) different morphologies, (ii) use/elimination of additives (to enable fast and reversible charge storage)[2].

1.3.7.2.1 Changing morphology:

The architecture and rational design of the electrode material are crucial in determining the ion diffusion channel length and the material's capacitive behaviour [2]. Supercapacitors' electrode materials have been developed and tested in a variety of configurations, from 0D particles to 3D frameworks [21].

Due to the variability of parameters and evaluation conditions, comparing the performance of electrodes with different dimensionalities is difficult. However, it may be inferred that there are distinct benefits and drawbacks for various dimensionalities. In contrast to zero-dimensional materials like particulate layers, where disconnected particles impede electronic conductivity and ionic transport, 1D structures like fibres, wires, and tubes are demonstrated to be effective materials to store charge due to their directional ionic and electronic transport [2]. The accessible space between structures with high aspect ratios cannot be precisely regulated in case 1D materials. While it is possible to deisgn the pore size to be smaller than 10 nm in 0D electrode materials to get superior electrolyte accessibility than 1D materials [21].

A feasible direction is to choose the dimensionalities, that can provide high surface area, capacitance, pathways for electronic and ionic conduction and performance stability.

According to formula [20].

$$\tau 0 = L^2/qD$$

where $\tau 0$ is the time constants, D is the diffusion coefficient, L is the diffusion distance, and q is a dimensionality-dependent constant ($q = 2$, 4, or 6 for one-, two-, or three-dimensional diffusion, respectively). As compare to 1D and 2D materials, 3D electrodes have a shorter ion diffusion time, which can enable improve rate capability [20].

3D open porous structures provide highways (transport routes) for electron conduction. [20] also the effective surface area and performance can be enhanced [13].

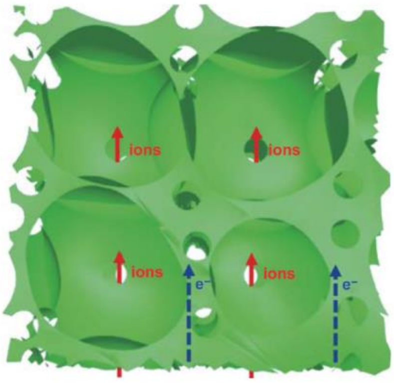

Figure 7: Electron and ion movement in 3D electrodes [20].

Careful design strategies i.e open porous structures for ion movement, and precise control of pore size can increase the ionic conductivity [21]. Hence, developing 3D structures with precise pore size distribution as electrode materials is quite useful.

1.3.7.2.2 Reduce or to eliminate additives/binders:

Reducing or eliminating binders and additives is one method for improving the electronic conductivity of electrode materials [2] as they provide efficient path to electrons for charge transport [21]. By growing the electrode active material directly onto a metal substrate, binder-free electrode materials can be produced [2]. This reduces the collector/electrode resistance [2] and enable effective electron transit between a current collector and an active material [21]

1.4 Chosen Alloy:

Because of their large capacity to store energy, which is almost greater by one order of magnitude than carbon-based electrodes, transition metal oxides are emerging as viable alternatives for capacitive electrodes [2] . Because to its low conductivity and limited surface area, the metal oxide supercapacitance is, nevertheless, smaller than theoretical expectations. So, we design NbTiVZr high entropy alloy that consist of four elements in equiatomic ratio.

Metals are carefully selected having high-melting points which are non-toxic, possesses high strength, resistance to corrosion, and resistance to softening at high temperatures [22]. Niobium oxide has high switching ability between various oxidation states such as +2 in NbO, +3 in Nb_2O_3, +4 in NbO_2 and +5 in Nb_2O_5 [2] , and Titanium improves cyclic stability with almost no fade in capacitance, while vanadium exhibit faradic reaction leading to increase in volumetric and areal capacitance[23]. So, the present study aims at coupling Niobium, Titanium, Vanadium and Zirconium to emphasize their potential as high entropy alloys for supercapacitor applications. Hence, they became potential aspirants in the field of supercapacitors.

As porous metal oxide have large surface area [18] because greater deployment of active material is exhibited leading to significant increase of capacitance[19]. So, porosity is introduced in different ratios in alloys. Selective dissolution would be employed to construct the porous alloys [24].

1.5 High entropy alloy:

It is generally used to design a new alloy by choosing one major element and considering minor amounts of alloying elements to attain specific properties. On the other hand, Cantor et al. [16] and Yeh et al. [22] designed new alloys that consist of 5 to 20 elements, in 2004 [16] forming one or more solid solution phases [6] where there was no longer major element unlike previously designed conventional alloys [16].The concentration of principal elements in HEAs typically range from 5 to 35 at% [22].

Due to the direct increase in the mixing entropy as the number of system components increases, multi-principal systems are also called high entropy alloys. Entropy is a measure of system's unpredictability and is made up of four basic components: Electronic randomness, magnetic dipole, vibrational, and configurational.

While there are more options for lattice structures as the number of elements increases in the system, configurational entropy is the primary factor in the case of high entropy alloys. In terms of configurational entropy alloys whose configurational entropy is higher than 1.5 R are called HEAs.

Conventional alloys mostly contain two or three elements, which restricts the compositional space for designing new alloys with improved properties. Traditional design methodologies has been revolutionized through the advent of multi-component HEAs [25], [26], [27].

A recent, ground-breaking advancement in materials science is the concept of high entropy alloy that has allowed us to break free from the limitations of material design and open endless possibilities in the field.

The performances of HEAs are thought to be governed by four "core effects": the high-entropy effect, the lattice distortion effect, the sluggish diffusion effect, and the "cocktail" effect. In the coming sections, they will be covered in more detail.

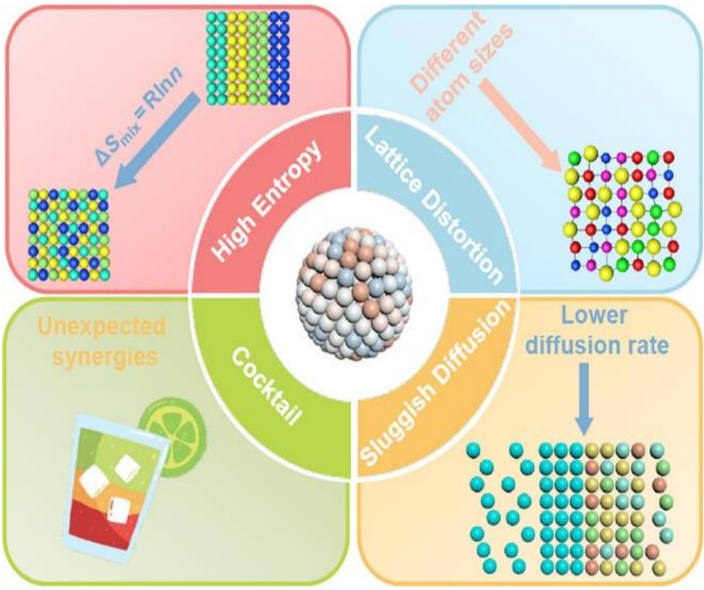

Figure 8: Core Effects of HEA's.

1.5.1 High entropy effect:

According to this effect when mixing entropy is high (especially configurational entropy), it would cause reduction in free energy of HEAs. As a result, at higher temperatures solid solution phases are formed. Because of high solubility between the HEA elements, number of phases present in it are less [28]. As shown in equation given below:

$$\Delta Gmix = \Delta Hmix - T\Delta Smix$$

Here, the variables T is temperature, H is enthalpy, and S is entropy. Higher entropy phases stabilize at higher temperatures, provided the temperature is high enough.

Order present in HEA decreases when the temperature rises. In the as cast state when the alloys are at low temperature it contains ordered phases which are converted into random solid solution with rise in temperature. At high temperature if the enthalpy of formation for intermetallic compound is high enough to combat the entropy effect, then it would be stabilized at higher temperatures. Entropy and enthalpy compete with one another to decide the phase formation [29].

1.5.2 Strong lattice distortion effect:

Various elements each having different sizes are present in the lattice of HEAs. The lattice distortion occurs due to these size differences. Smaller atoms have more space around and larger ones push away their neighbors' atoms. Distortion in the lattice of HEAs results in strain energy which in turn raises the total free energy of High entropy lattice. Properties of high entropy alloys are also affected because of it e.g the strength of solid solution increases because dislocation movement is prevented by lattice distortion [30].

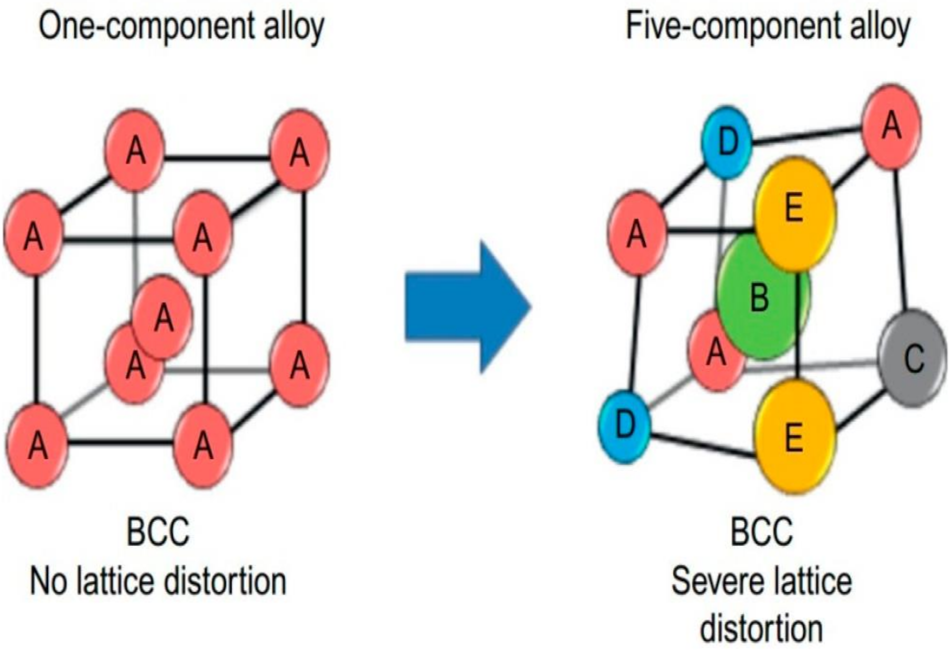

Figure 9: High entropy alloys' lattice distortion.

1.5.3 Sluggish diffusion effect:

When compared to conventional alloys phase change in HEA as well as diffusion is sluggish [31]. This can be seen in two different ways.

First, each lattice site in HEA has somewhat distinct neighboring atoms. Because of this, the neighbors earlier and later an atom jump into a vacancy are different. Atomic configuration variations cause different bonding, and as a result, each site's local energy is different. When an atom jumps into the site of low energy it becomes trapped there and to jump out of that site becomes difficult for it. Whereas when an atom jumps into site of high-energy state, the atom has a more chances of returning from it. Either of these situations slow down the diffusion process. Solute concentration is slow in case of conventional alloys so in that case the neighboring atoms remain same before and after an atom jumps into the vacancy [32]. Second, each element of a HEA has a different diffusion rate. Some elements (such those with high melting points) are less successful at jumping into vacancies because they are less active than other elements.

Phase change only takes place when many kinds of elements move together, but the elements that move slowly impedes the transformation and slow down the process of phase transformation [26], [33], [34]. Because of this slow diffusion process in case of HEAs they show excellent performance as diffusion barriers [35]. Slow diffusion and low rate of phase transformation are responsible for the good creep strength, strength at high temperature, and provide structural stability.

1.5.4 The cocktail effects:

The characteristics of HEAs are correlated with those of its constituent elements. For instance, adding light components reduces the density of the alloy. Yet, in addition to the characteristics of the individual components, consideration should also be given to how the component elements interact with each other. Reactions between different elements of HEAs, lattice distortion, and average properties of all the elements of which HEA is made up all together effect the overall macroscopic properties of these multicomponent high entropy alloys [27].

1.6 Research Objectives:

The following are the main objectives of this research project:

- Design the nontoxic TiNbVZr high entropy alloy through Thermo Calc software.
- Synthesis of TiVNb alloy by Vaccum Arc Melting process.
- Characterization of the as cast alloys by using the Scanning electron microscope, EDS elemental mapping Analysis and X-ray diffraction.
- Dealloying of the as-cast samples to produce the NbTiVZr foams, formed by removing the filler element.
- Characterization of developed foams in various percentage of porosity (0-15%) by using SEM, Elemental mapping and XRD.
- Electrochemical characterization of the foams is studied by CV, GCD and cyclic stability for capacitance and charge storage.

Chapter: 2

Literature Review

In recent years, researchers have been more interested in supercapacitors. Thanks to the recent advancements in electrode material and technology, the difference between capacitors and batteries is narrowed by supercapacitors. Figure 10. displays materials used in recent years as well as the number of supercapacitor research projects carried out throughout the last two decades.

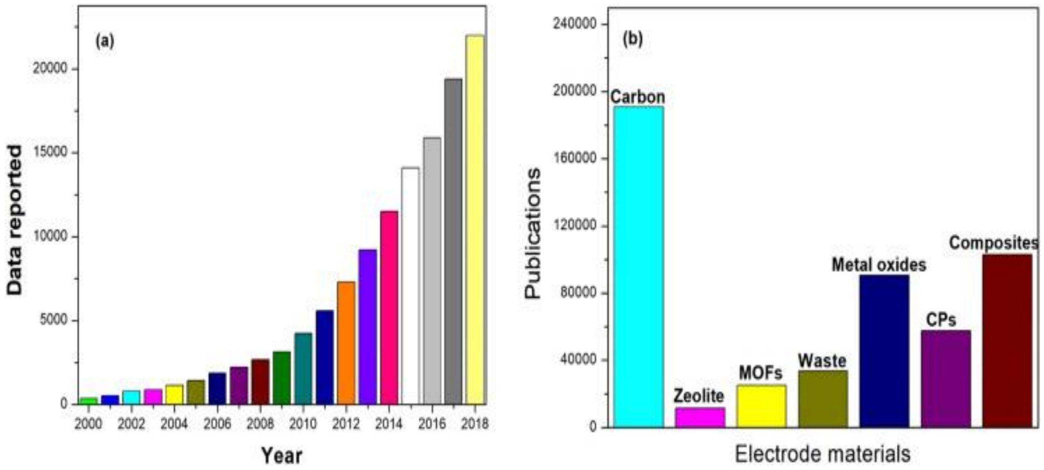

Figure 10: (a) Number of research publications (2000-2018) on supercapacitors. **(b)** Publications on electrode materials [36].

2.1 Conventional Electrode Materials for Supercapacitors:

The material to be chosen as supercapacitors electrode is crucial since it affects the electrical properties [3]. To improve the capacitance, new electrode material for supercapacitors should have high surface area, good conductivity, adjustable pore size [11], good surface functionality, permeability of electrolyte solution and wetting of electrode [3]. Those electrode materials should be developed that can store large amounts of energy and can collect lots of electrons for supercapacitors.

Suitable choices for electrode materials include carbon materials, conducting polymers and also metal oxides or hydroxides are thoroughly investigated by researchers.

2.1.1 Carbon Based Materials:

Supercapacitors electrodes are made up of , a variety of carbonaceous nanomaterials have been employed, including carbon nanotubes, activated carbons, carbon onions and carbide-derived carbons [13].

As an electrode materials for supercapacitors, CMs have emerged as prime choice because of their superior surface area, changeable porosity and enhanced electrical conductivity [37]. A significant variety of methods for creating porous CMs have been reported [38]. Moreover, CMs can achieve increased pseudo capacitance, electrical conductivity, and surface wettability by adding heteroatoms. [39]. However, carbonaceous compounds are usually difficult and expensive to prepare. The preparation methods involve corrosive chemical chemicals that not only damage the equipment but also pollute the environment [38]. Also the charge storage capacity is limited in carbon based materials [15].

2.1.2 Polymer Based Materials:

Conducting polymers (CPs) were initially used in supercapacitors in the last decade of twentieth century [40]. Their performance is better when these materials are used as electrode for asymmetric capacitors [41] Due to unique physicochemical qualities the electrically conductive polymers (CPs) make them a suitable candidate material for supercapacitors electrode [42].

They offer design flexibility. As compared to electrodes that are made up of metal oxides, conducting polymers electrode price is normally similar or less than them. Additionally, the corresponding series resistance of these polymeric electrodes is smaller. Other benefits of conducting polymers are their tailorable morphology and strong inherent conductivity of 1-500 S cm^{-1}. Conducting polymers also have adaptable morphology and high intrinsic conductivity of 1-500 S cm^{-1} [7]. Polythiophene derivatives among the CPs have undergone substantial research for their use in supercapacitors [43]. N-doped polythiophene, however is not very stable to moisture and oxygen, and it also has lesser conductivity when compared to p-doped polymer [44].

In case of electrodes that are made up of polymers diffusion of ions into the bulk of material is very slow, that causes their slow charge and discharge. This is one of the disadvantage of these polymer electrodes [7]. Electrochemical stability of polymer based electrode is also poor [12]. They also have a short cycle life and are easily oxidized [42].

2.1.3 Metal Oxides:

As potential supercapacitor electrode materials, transition metal oxides including MnO_2, RuO_2, IrO_2, V_2O_5, Ni $(OH)_2$, TiO_2, MnO_2, NiO, SnO_2, Co_2O_3, FeO and MoO are analyzed [18].

Electrode that are made up of metal oxides are able make supercapacitors having both high energy and power density because they have low resistance and high capacitance values.

Because to the high capacitance due to the reversible redox reaction [1]at the surface of metal oxide, they exhibit higher energy storage capabilities [6].

Due to their multiple oxidation states, transition metal oxides (TMOs) are attractive candidate for supercapacitor applications [17]. Energy storage ability of transition metal oxides (TiO_2, Nb_2O_5, RuO_2, SnO_2, V_2O_5, Co_2O_3, and FeO)[16] is higher than carbon electrodes and this makes them promising candidates for supercapacitor electrodes [2]. Yet, because of low conductivity and inadequate surface area, metal oxide has a lower capacitance than theoretical expectations [18].

2.2 High Entropy Alloys:

Due to limitation of conventional materials, researchers are looking at novel materials to develop a viable replacement for existing electrode materials. High entropy alloys that are new class of multicomponent alloys was designed and developed in 2004 because of the restricted space available in the design and development of binary and ternary alloys to attain desirable properties [25].

Since their discovery in 2004, a tremendous amount of high entropy alloys has been created. Non-toxic refractory metals like Nb, Ti, V, and Zr are suitable candidates among the HEA alloys for use in supercapacitor applications as electrode materials. Metals are carefully selected having high-melting-point metals which possesses high strength, non-toxic, corrosion resistance and high temperature softening resistance [22]. Niobium oxide has high switching ability between various oxidation states including +2 in NbO, +3 in Nb_2O_3, +4 in NbO_2 and +5 in Nb_2O_5 [2] , and Titanium improves cyclic stability with almost no fade in capacitance, while vanadium exhibit faradic reaction leading to increase in volumetric and areal capacitance[23].

So, the present study aims at coupling Niobium, Titanium, Vanadium and Zirconium to emphasize their potential as high entropy alloys for supercapacitor applications. Hence, they became potential aspirants in the field of supercapacitors. Because of the considerable lattice distortion effect resulting from the integration of different-sized component pieces into a solid solution phase, these high entropy alloys have remarkable hardness and mechanical strength.

High entropy alloys are a great choice for supercapacitor applications as an electrode material because of the following characteristics:

(1) HEA when used as electrode, have good structural ability, and thus prevents its expansion and contraction. This structural stability improve cyclic stability and other electrochemical performances of HEA when it is used as electrode material for supercapacitors [11].

(2) HEA has the cross linked structure, which facilitates the movement of electrons and ions in charge discharge process [11].

(3) Low electrode impedance and resistance are produced as a result of less active material being shed during charge and discharge because the high entropy alloy reduces the material’s volume expansion [11].

(4) HEA having the pore structure not only provides the route for electrolyte ions but also the large number of electroactive sites [11].

The HEA has gained potential as a material for making super capacitors since it complies with these specifications. Unfortunately, relatively few attempts have been undertaken thus far to investigate the electrochemical catalytic or storage property.

2.3 Comparison of Electrochemical properties between Conventional and High Entropy Alloys:

2.3.1 Conventional Materials:

Activated carbon obtained from pistachio nutshell deliver the capacitance of 20.1 mF/cm^2 at 2 mV/sec [45]. C-MEMS electrodes (tested in a two-electrode set-up) prepared by microelectromechanical (MEMS) system shows the areal capacitance of 0.046 mFcm-2 (at 20 mVsec^{-1}) [13]. Enhanced areal capacitance upto 330 μF/cm^2 (at 0.1 Ag$^-$

^{1}) in H_2SO_4 can be achieved through diethylamine carbon micro-spheres having ultra-micropores prepared by low temperature solvothermal route [46]. Wang et al. in 2019 synthesizes Mn-decorated Zr-MOF-CNT nanocomposites by solvothermal deposition method, that shows the capacitance value of 4.9 mF/cm^{2} at current density of 50 μA/cm^{2} in the potential window of 0-1V [47]. By merging the two-beam-laser-interface (TBLI) system with the masking approach in 2021, Yan Fu creates the Planar TBLI-RGO. It exhibit 3.97 mF/cm2 capacitance at 10 mV/sec in the 0 to 1V potential range. [48]. PVDF/graphene electrode synthesized by Thong le et al. in 2021 displays the areal capacitance of 0.0059 mF/cm^{2} (at 100mV/sec) [49].

The capacitance values of PProDOT-EtO-BZA formed by electro polymerization is 20.8 mF cm^{-2} (20 mVsec^{-1}) [42]. At 200 mA g^{-1}, Polymer-derived carbons (PDCs) i.e., CXH7 (carbons reduced at 700 ºC) shows capacitance of 252 μF cm^{-2} (ΔV=0.25 to 0.85V) [50]. PVA/PANI/ZrOx composite electrodes were synthesized by Myasoedova et al. in 2020 by chemical polymerization of aniline in the presence of hydrochloric acid. The composite displays a 39 mF/cm2 capacitance at 0.075 mA/cm2 capacitance in the potential range of 0 to 0.5V [51].

The VN/CNT electrode was synthesized by Ouldhamadouche et al. in 2017 and exhibits a capacitance of 37.5 mF cm-2 in 2 mV sec-1.[52]. In 2019, Durai et al. fabricated VN films that's shows the capacitance of 27 mF cm^{-2} (10 mV/sec) in the potential window of -1 to 0V [53]. Porto et al. in 2022 developed VOxNy and TiOxNy powder electrodes through conventional nitridation method. At 10 mV/sec, the produced powders exhibit capacitances of 0.3 mF/cm^{2} and 0.05 mF/cm^{2}, respectively. [54]. Achour et al. in 2017 synthesized TiVN2 films through DC co-sputtering method, that exhibits 24 mF cm^{-2} capacitance at the scan rate of 2 mV/sec [5]. Ozkan et al. in 2017 developed the TiO_2 nanotubes coated with Nb_2O_5 nanocrystalline layers (TiO_2/Nb_2O_5) that gives 37 mF cm^{-2} capacitance value at 1mV sec^{-1} (ΔV= 0 to 0.6V) [55]. In 2015 Anchor et al. studied TiN films synthesized through reactive DC sputtering that at scan rate of 2 mV sec^{-1} exhibits the capacitance value of 12 mF cm^{-2} [56].

Table 3: Conventional carbon, polymer, and Metal oxides/ nitrides-based electrode materials for supercapacitors.

S. No.	Material	Electrolyte	Voltage Range	Scan Rate	Capacitance	References
1	**Mn-decorated Zr-MOF-CNT nanocomposites**	0.1 M Na_2SO_4	0 to 1V	50 μA/cm^2	4.9 mF/cm^2	[47]
2	**Planar TBLI-RGO**	PVA–H_3PO_4	0 to 1V	10 mV/sec	3.97 mF /cm^2	[48]
3	**PVDF/graphene**	1M H_3PO_4	0V to 1V	100 mV/s	0.0059 mF/cm^2	[49]
4	**VN/CNT electrode**	0.5M K_2SO_4	-0.1 to 0.4V	2 mV/sec	37.5 mF /cm^2	[52]
5	**PVA/PANI/ZrOX**	3 M KOH	0 V to 0.5 V	75 μA/cm^2	39 mF/cm^2	[51]
6	**VN**	1M KOH	-1 to 0V	10 mV/sec	27mF/cm^2	[53]
7	**VOxNy powder** **TiOxNy powder**	1M KOH 1M KOH	-1.2 to 0V -0.6 to 0.2 V	10 mV/s 10 mV/sec	0.3 mF/cm^2 0.05 mF/cm2	[54]
8	**TiVN2**	1M KOH	-1.3 to 0 V	2 mV/sec	24 mF/cm^2	[5]
9	**TiO2/Nb2O5 NTs**	1M H2SO4	0 to 0.6 V	1 mV/sec	37 mF/cm^2	[55]
10	**TiN film**	0.5M K_2SO_4	-0.2- 0.5 V	2 mV/sec	12 mF/cm^2	[56]

2.3.2 High entropy alloys:

The electrochemical performance of multicomponent oxides along with its electrical conductivity is higher than that of oxides that have single component. Because of this reason HEA having multiple components could be used as material for supercapacitor electrodes [6].

However, the use of HEMs for energy storage has only recently been studied, and further research is required to fully comprehend the relationships between their structure and performance [57].

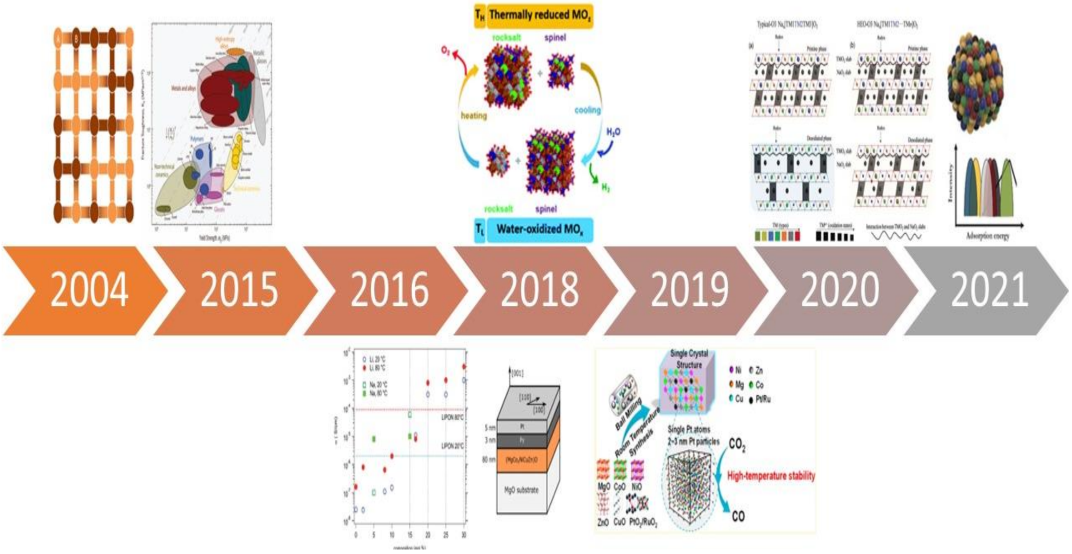

Figure 11: HEM’s roadmap for current uses in the energy sector [57].

Before 2015, HEMs were mostly employed as structural materials (Gludovatz et al., 2014).[58]. Rost et el. in 2015 discovered the entropy stabilized oxides (HEOs) [59]. In solid electrolyte, many HEMs have been produced and utilized, by Berardan et al. in 2016 [60], exchange coupling by Meisenheimer et al. in 2017 [61], water decomposition by Zhai et al. in 2018 [62], COOr/CO_2RR catalyst by Chen et al., in 2019 [63], Li- ion battery by Wang et al. in 2019 [64], and Na-ion battery in 2020 by Zhao et al. [65].

Materials with specific qualities, such as strong ionic and electronic conductivity and high capacity, are required for supercapacitor applications. These demands might be met by the HEOs' cation tunability [57].

Kong et al. dissolved the selected HEAs in H_2SO_4 solution and were able to create nano porous HEAs. Without the addition of binder, the AlCoCrFeNi HEA having the nonopores shows the high 700 F/cm^3 volumetric capacitance along with high cyclic stability for 3000 cycles. The great performance could result from its interconnected larger pore channels that provide large surface area [6].

Many different HEMs with large surface areas have been created for use in supercapacitors. For example, Jin et al. uses mechanochemical assisted soft urea method for **(VCrNbMoZr)N** HEN synthesis. When employed as electrode material, at 100 mV/sec, HEN in 1M KOH displays 78 F/g capacitance value [66].

On super aligned electrospun carbon nanofibers, Xu et al., synthesized unfiorm quinary FeNiCoMnMg (30 nm) and FeNiCoMnCu (50 nm) NPs via CTS. The later exhibits specific energy density of 21.7 Wh/kg and high capacitance of 203 F/g [67]. At 10 mV/sec (TiNbTaZrHf)C that was prepared by facile electrochemical process shows 95.2 F/g capacitance value [57].

The use of High entropy alloys in the energy related applications are still in their infancy. High entropy alloys have been extensively used in the past due to their extraordinary mechanical properties but the use of HEA especially refractory high entropy as material for electrodes is a new research area. In the current study, to the extent that we know, porous refractory high entropy alloys prepared through the dealloying process would be discussed for the first time for supercapacitors applications.

Chapter: 3

Experimental techniques

In this chapter, experimental methods and characterization techniques are discussed. Alloys of different compositions are designed and manufactured in arc suction melting furnace. As-Cast alloys were obtained in the form of buttons. All the alloys were cut through the EDM wire cut machine. Microstructural characterizations i.e SEM and XRD were performed on the as cast samples.

Samples were then dealloyed in an acidic solution to remove the filler element. Microstructural Characterization i.e SEM and XRD were done on the dealloyed samples. Steps involved from preparation of alloy to the complete characterizations are as follows.

- Alloy preparation
- Cutting through EDM wire cut
- Microstructural Characterizations
- De-alloying
- Microstructural Characterization
- Electrochemical Characterization

3.1 Preparation of Alloy:

Alloys were designed and then prepared in arc suction melting furnace. Highly pure metallic chips were used as raw materials for the preparation of alloy. Arc suction melting furnace has the water-cooled copper hearth with five crucibles and tungsten electrode is present in it. Argon gas was injected after creating a vacuum of 10^{-5} torr in the chamber. Tungsten electrode acts as cathode while copper hearth acts as anode. Alloys were prepared in Arc suction melting furnace as shown in fig 12.

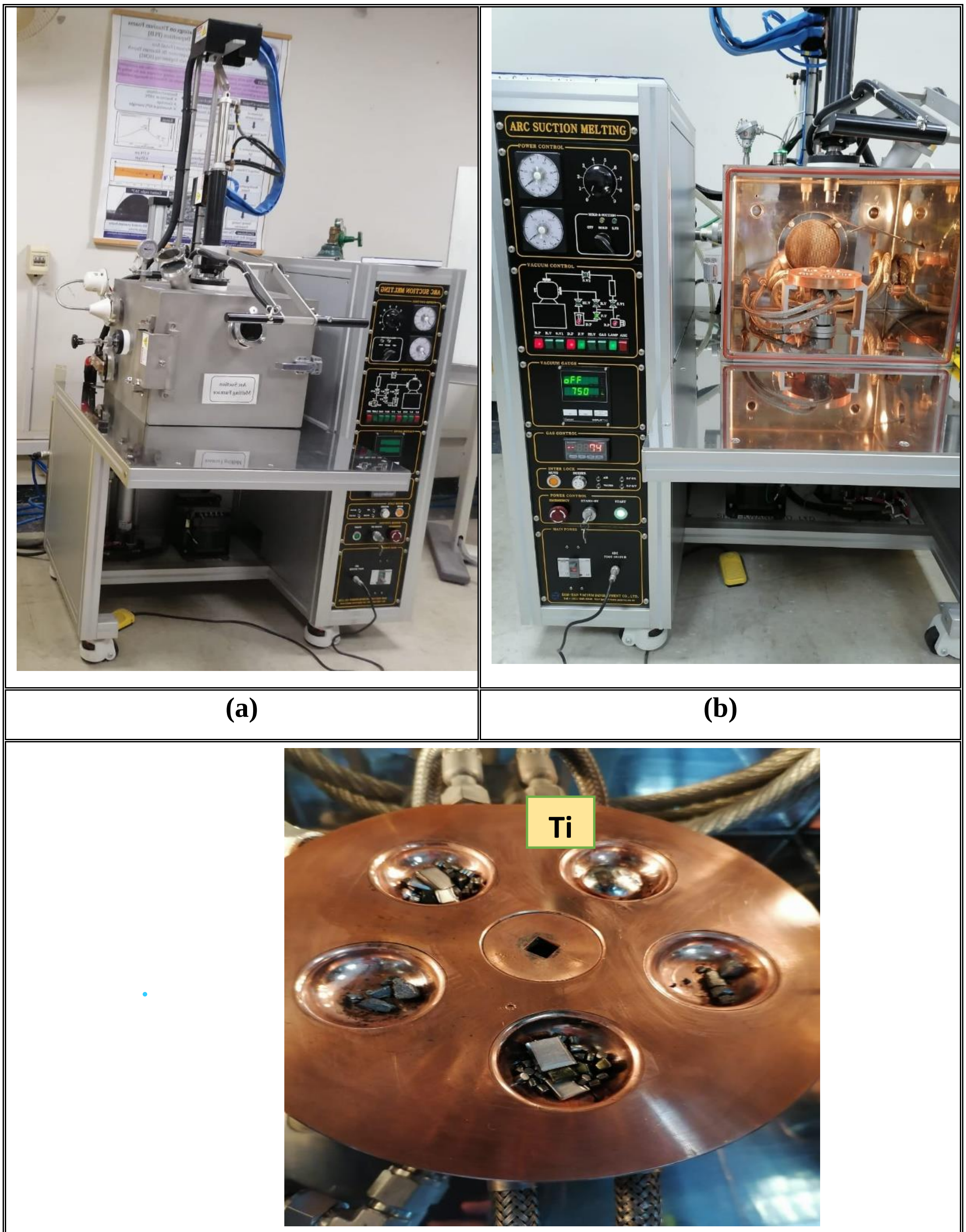

(a) **(b)**

(c)

Figure 12: (a) outer and (b) inner view of Arc suction melting furnace and (c) cupper crucibles.

Prior to melting alloys, a titanium getter is placed in the arc furnace to eliminate all the oxygen from the chamber. Metal chips are placed on the crucibles. As the arc hits on metal chips, large current passes through it and melting takes place. Alloy solidification takes place and alloy is flipped over with the help of tweezers and remelted at least five times without breaking the vacuum to ensure homogeneity. Button shape alloy was formed as shown in fig 13.

Figure 13: Button shape metallic sample produced from arc suction melting furnace.

EDM wire cut then cut the metallic buttons into desired shapes to perform further characterization.

3.2 Grinding and polishing

Samples obtained from EDM wire cut were then hot mounted by using the Bakelite powder at the temperature 1800 ºC on the mounting press as shown in fig 14 (a).

(a) (b)

Figure 14: (a) Mounting press machine **(b)** mounted sample.

Mounted samples were firstly grinded on P400 to P2000 grit sized silicon carbide emery papers. Samples were then polished on polishing cloth using 0.5 µ alumina slurry to obtain the scratch free samples. The grinding and polishing machine used in the preparation of sample are shown in fig. 15 (a). Samples were then sonicated to clean and remove the alumina residue from samples fig. 15 (b).

(a) (b)

Figure 15: (a) Grinding and Polishing Machine, (b) sonicator.

3.3 Samples Characterization:

3.3.1 Scanning electron microscope:

Scanning electron microscopy (SEM) analysis was performed on prepared (as Cast) samples. The working principle of SEM is the application of kinetic energy to generate signals from the collision of electrons. It focuses a small electron stream on the test specimen's surface resulting in emission of electrons and photon from surface of sample. The knocked off electrons and photons are then focus on detector. The brightness of the CRT (cathode ray tube) is modulated by the detector's output. As a result, every specimen site where an electron beam was concentrated has a corresponding point plotted on a cathode ray tube. SEM analysis give us information about surface morphology, crystallography, chemical composition, and planes orientation. The operating principle of SEM is shown in schematic below (figure 16).

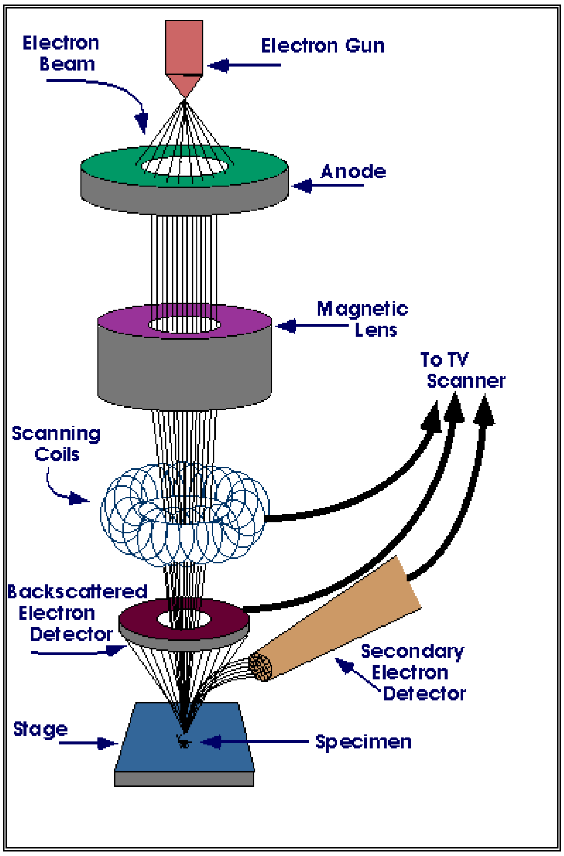

Figure 16: Schematic of scanning electron microscopy.

SEM model (JEOL-JSM-6490LA) equipped with EDX and Elemental Analyzer was used to carry out SEM analysis. Image of SEM analyzer used in this study is given below in fig 17.

Figure 17: Scanning electron microscope equipped with EDX and Elemental Analyzer.

3.3.2 X-ray diffraction Analysis:

To examine the various crystalline phases, present in test sample X-ray diffraction analysis is used which is a nondestructive method. Working principle of XRD consists of constructive interference between crystalline sample and monochromatic X-rays. Cathode tube, sample holder, and X-ray detector are the three main components of XRD. The x-ray tube's filament is heated to produce monochromatic electrons, which are then propelled toward the target metal. The characteristic x-rays produced strike the surface of the sample, reflect, and are detected by an x-ray detector. Crystal is composed of layers and planes. Therefore, constructive interference occurs when x-rays with wavelengths identical to those planes reflect, according to Bragg's law (when the angle of incidence and angle of reflection are equal, diffraction takes place), and those "Bragg’s reflections" are detected by the detector. XRD provides data on crystallinity and phases. Fig.18 shows an XRD schematic.

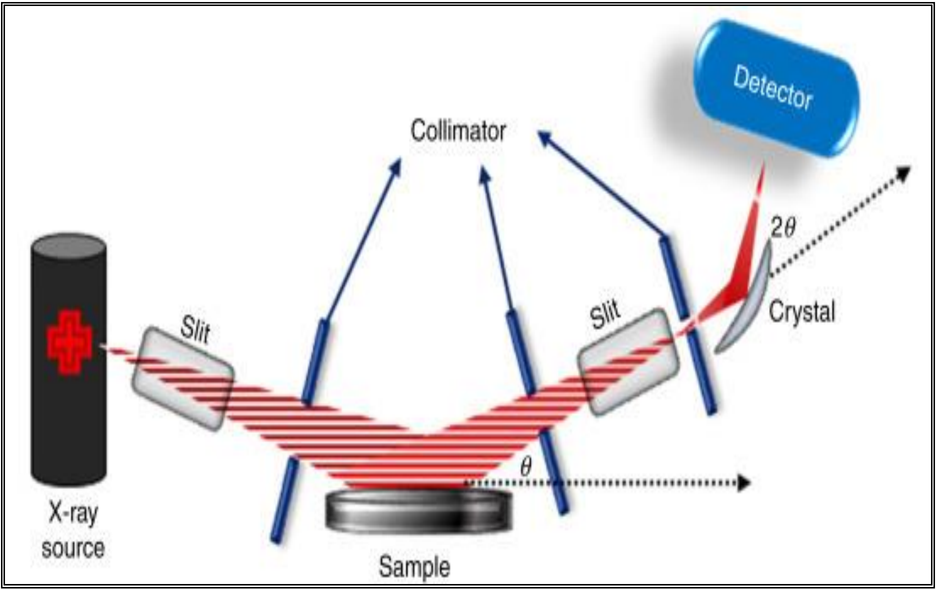

Figure 18: Schematic diagram of XRD.

Samples of 1 mm thickness were cut through EDM wire to ensure even geometry. Samples were then grinded for XRD analysis. XRD used in this study is (D2, Phaser Bruker).

3.4 Dealloying Process:

Dealloying process is used to introduced porosity by removing the filler element to make metallic foam. Before dealloying weight of each alloy is measured using in weighing balance. Solution of 25ml deionized water and 25ml nitric acid is prepared for each sample separately in 100ml glass beakers. After that for 24 hours samples were immersed in the solution and immersion time was noted down. Samples were taken out of solution after 24 hours and sonicated in ethanol and water for 2 minutes each. After sonication samples were dried on hot plate (30 min: 130 ºC). Samples were weighed again, and mass loss was calculated. Fig.19 (a-d) shows the subsequent steps involved in the delaying process.

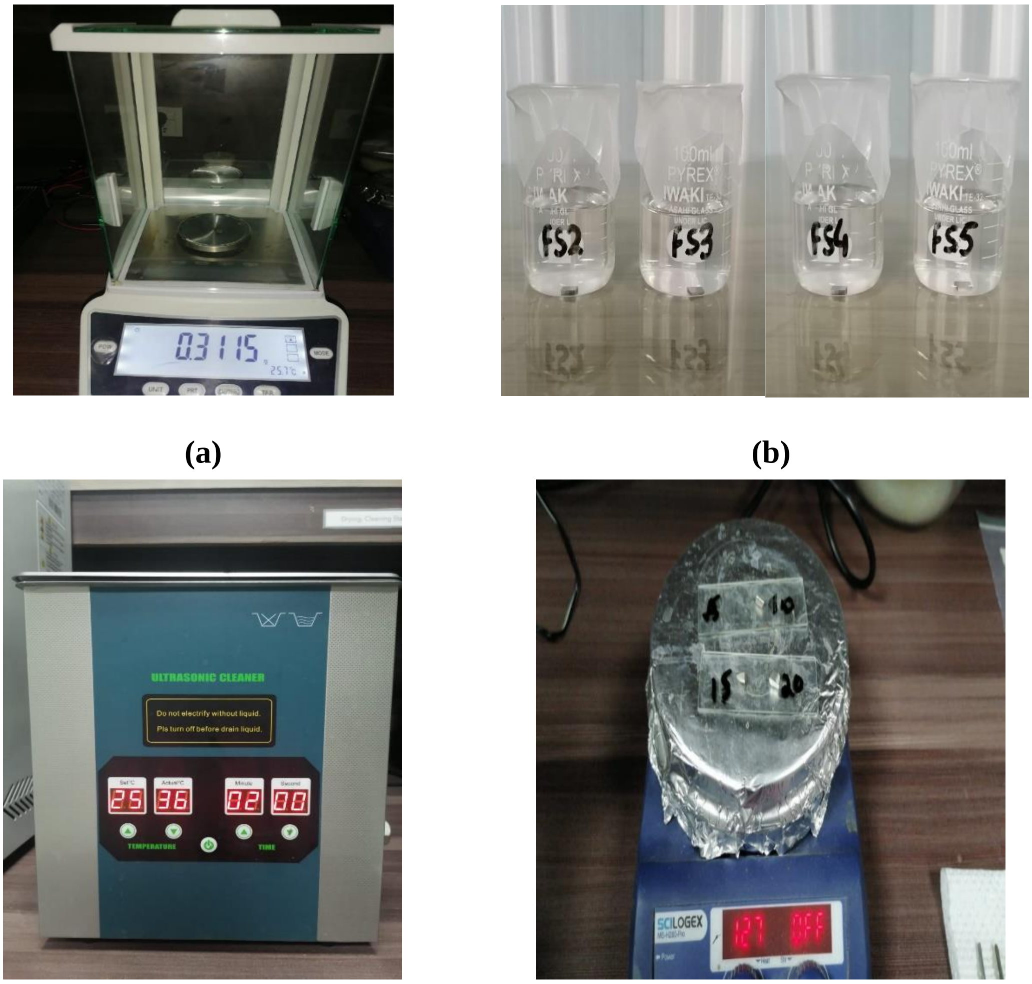

(a) **(b)**

(c) **(d)**

Figure 19: Subsequent dealloying steps (a) weighing of alloy (b) immersion of sample in solution (c) sonication and (d) drying of foam samples.

Microstructural characterization of the alloys was performed again, to compare the microstructural changes before and after the dealloying process. XRD data comparison provides information regarding the removal of the filler element. While SEM results comparison shows the change in microstructure that occurred after the de-alloying procedure.

3.5 Electrochemical characterizations:

3.5.1 Electrochemical Workstation:

Gamry workstation Interface (1010 E) and Biological VSP are the research-grade Potentiostat present in SCME. Every equipment consists of workstation, electrochemical cell, computer hardware and software system. They are used for variety of applications, including:

- Material impedance spectroscopy
- Battery testing

- Liquid conductivity
- Fuel cell and biofuel cell
- Corrosion testing
- Electrochemical deposition of thin film
- Photovoltaics and sensors
- Capacitor and supercapacitor testing
- Cyclic Voltammetry Analysis
- Galvanostatic charge-discharge Analysis
- Electrochemical Impedance Spectroscopy

Cyclic voltammetry (CV) and EIS analysis were carried out on Gamry workstation Interface (1010 E) while GCD analysis was performed on Biological VSP.

3.5.2 Cyclic Voltammetry (CV) Analysis:

The simplest technique to evaluate the electrochemical behaviour at laboratory scale is cyclic voltammetry. CV system consists of three electrodes i.e reference electrode, working electrode and counter electrode, which is then used to analyze the oxidation and reduction (redox) reactions occurring at electrolyte and electrode interface. In CV, on the WE and RE, potential is applied and between counter and working electrode resulting output current response is recorded. CV curve is the resulting current (I) of WE vs. potential (V). Counter electrode is mostly platinum while most used RE are SCE (saturates calomel electrode) and Ag/AgCl (silver/silver chloride). Electrolyte must possess good conductivity and its purpose is to provide ions. Different materials show different responses in supercapacitors. EDLC gives rectangular curves whereas pseudocapacitors give oxidation and reduction hump during forward and reverse scan as presented in Figures 20(b) and (c), respectively.

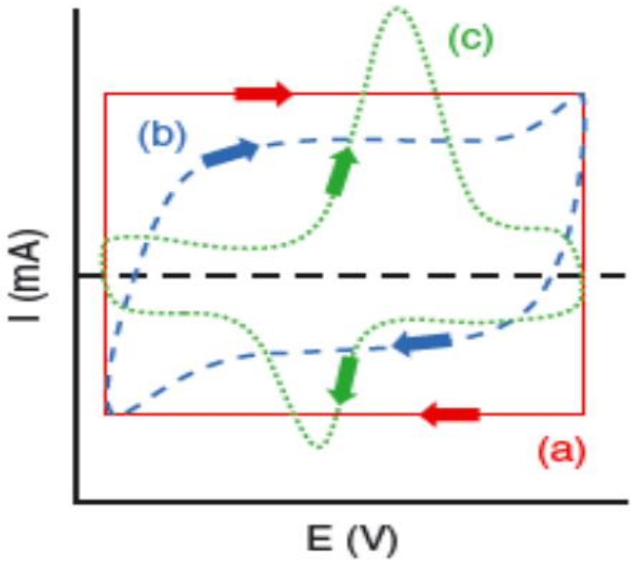

Figure 20: CV plot of (a) Ideal capacitor with perfect rectangular shape (b)EDLC material with near rectangular shape(c)Pseudo capacitor with oxidation and reduction peaks [68].

3.5.3 Galvanostatic Charge-Discharge Analysis (GCD):

GCD is common method to analyse the charging and discharging behaviour of supercapacitors as well as batteries. GCD measures potential vs. time at constant current. The material must be charged and discharged once for a full cycle to complete. Like CV, the GCD curves of an EDLC and a pseudocapacitors are different. EDLC materials show very little IR drop and have linear curves of during charge discharge cycles. Linear response indicates the absence of redox reactions, and that charge storage is physical adsorption of charges at electrode inference. In case of GCD, IR drop is large and shows nonlinear curve. The non-linearity in case of pseudocapacitors refers to the charge storage mechanism which take place due to oxidation and reduction reactions. Figure 21. shows the GCD curves for EDLC and pseudocapacitors.

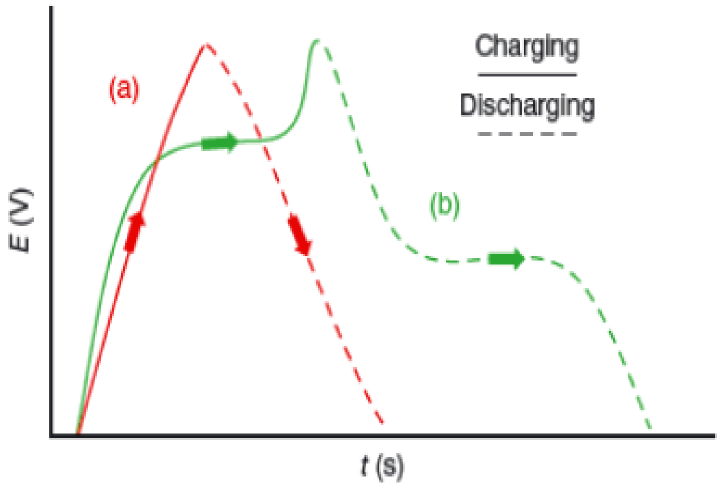

Figure 21: GCD curves of (a) EDLC (b)Pseudo capacitor [68].

3.5.4 Cyclic Stability:

Cyclic stability is an essential parameter for energy storage devices. Multiple charge discharge cycles are performed to check the cyclic performance of supercapacitors. To examine the material's capacity retention, 500–10,000 charge–discharge cycles are normally performed on a lab scale.

3.5.5 EIS Analysis:

EIS calculates the material’s impedance. It measures the dielectric characteristics, as a function of frequency. The Nyquist plot is designed to be based on the equivalent circuit (fig.22a) as a response of the system. Where, Rct is charge transfer resistance or polarization resistance, Re is series resistance at working electrode electrolyte interface, Warburg impedance depends on diffusion of reactants whereas, at the interface of the electrolyte and electrode, there is a double layer capacitance called Cd.

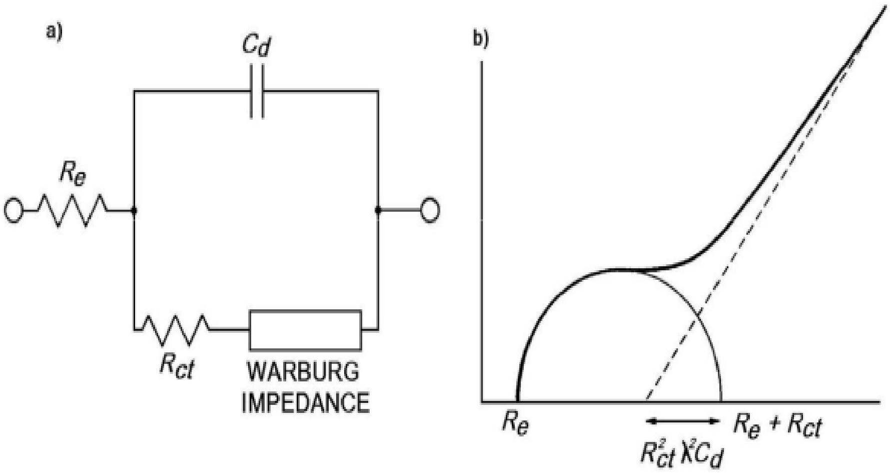

Figure 22: EIS (a) Equivalent circuit diagram (b)Nyquist plot [69].

3.5.6 Electrochemical characterization:

Electrochemical characterization of the developed foams was carried out and results were compared with base alloy NbTiVZr. Open Circuit Voltage (OCP) was performed for 1800 seconds to stabilize the sample in electrolytic solution before testing. On the Gamry workstation Interface (1010 E), electrochemical tests were performed i.e CV, GCD analysis, EIS and Cyclic Stability. CV tests were performed at 2, 10, 20, 30, 50, 80 and 100 mV/sec scan rates while GCD analysis was performed at current density of 100, 300, 500, 700, 900, and 1000 $\mu A/cm^2$. With an amplitude of around ±10V, EIS was carried out and a frequency limit of 100,000 Hz to 0.01 Hz. Equivalent circuit was designed according to the system in gamry software and impedance data was analyzed by fitting the designed equivalent circuit. of Three- electrode assembly was used for electrochemical testing. 1M Na_2SO_4 is used as an electrolyte. Platinum wire was used as counter electrode while Ag/AgCl was used as reference electrodes, while the testing samples was used as working electrode with an exposed area of 0.49 cm^2.

Chapter: 4

Results and discussion

In present study high entropy foams were developed for supercapacitor applications. The capacitance mostly obtained for batteries and fuel cells is higher than that of supercapacitors. Whereas the capacitance of supercapacitors is higher than that of conventional capacitors. To overcome the problem of low capacitance in the case of supercapacitors research has been carried out on novel materials used as electrodes. So, in the previous section, various techniques have been discussed in which as-cast high entropy alloys were developed in arc suction melting furnace and its microstructural characterizations were performed by using SEM and XRD. To understand the effect of dealloying on microstructural change in the generated foams, microstructural characterizations were again performed after the dealloying procedure.

4.1 Alloy design:

Metals Nb, Ti, V, Zr were carefully selected having high-melting-point metals which possesses high strength, non-toxic, corrosion resistance and high temperature softening resistance [22]. Niobium oxide has high switching ability among various oxidation states such as +2 in NbO, +3 in Nb_2O_3, +4 in NbO_2 and +5 in Nb_2O_5 [2], and titanium improves cyclic stability with almost no fade in capacitance, while vanadium exhibits faradic reaction leading to increase in volumetric and areal capacitance [23]. Study of binary phase diagram shows that all the elements have the negative enthalpy of mixing with each other that ensures complete solubility and homogeneity in the liquid and solid states respectively. To create the porosity in cast alloys a filler element is needed that demonstrates total solubility in molten state with all the other elements (Nb,Ti,V,Zr) and separation into interdendritic regions on solidification. Binary phase diagram of all the selected elements is studied with number of elements from periodic table and yttrium was selected as filler element because of its positive enthalpy of mixing with other elements. Therefore, yttrium was completely soluble with selected elements in molten form and completely insoluble in solidified foam. Therefore, pseudo binary phase diagram of (NbTiVZr)x-Y(1-x) was calculated with Thermocalc software using the TCHEA database. Five different high entropy alloys were designed:

- S1-NbTiVZr
- S2-(NbTiVZr)0.95-Y0.05
- S3-(NbTiVZr)0.90-Y0.10
- S4-(NbTiVZr)0.88-Y0.12
- S5-(NbTiVZr)0.85-Y0.15

S1 was used as base alloy. As cast alloys S2, S3, S4 and S5 alloys were then converted into foams and designated the names FS2, FS3, FS4 and FS5 respectively. As shown in fig. 23, designed compositions that were superimposed on the pseudo binary phase diagram.

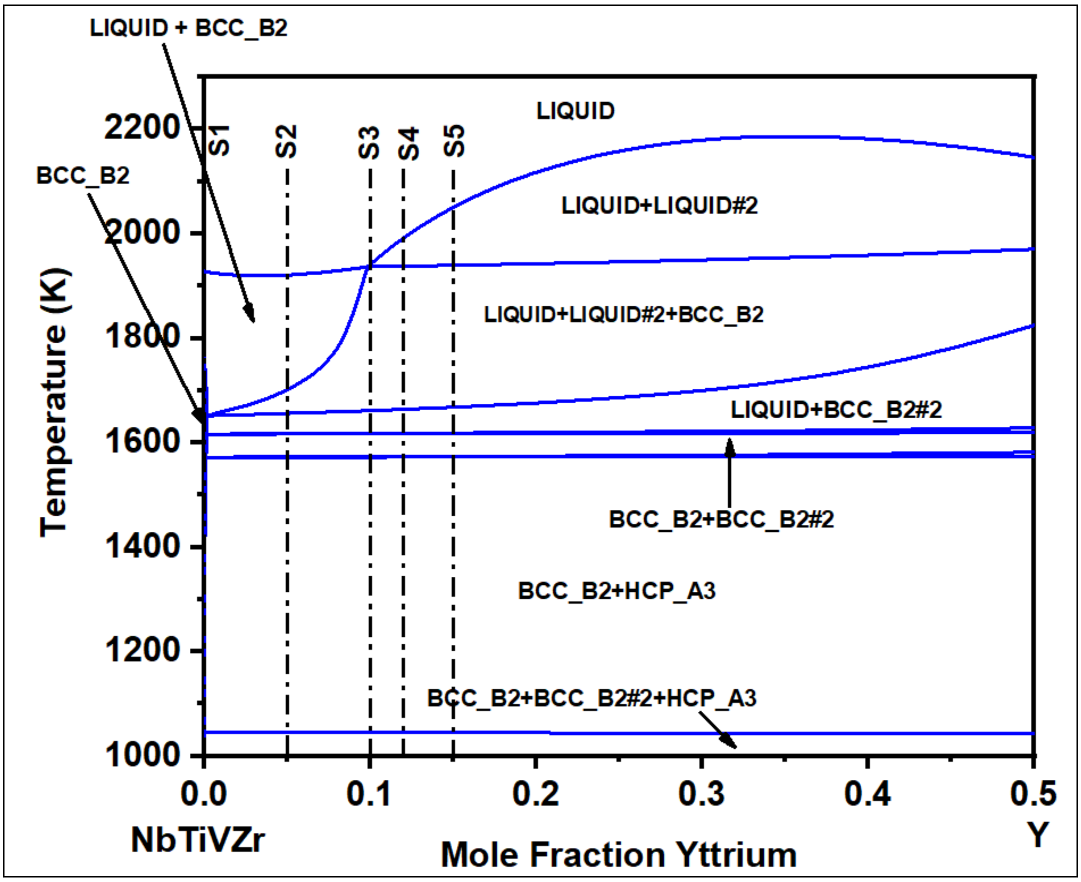

Figure 23: Pseudo binary phase diagram of temperature vs. mole fraction of Yttrium.

All of As Cast alloys have different compositions on the basis of different concentration of filler element. Porous alloys (foams) were developed by removing the filler element through chemical dealloying process. Dealloying agent was carefully selected that can only react with and dissolve filler elements without reacting with the remaining alloy elements. It was predictable from phase diagram that yttrium will move into inter-dendritic regions due to its complete separation in the solidified state. 3D porous structure is expected to be form by removing the filler element from interdendritic regions through chemical dealloying process. To conform our assumptions, microstructural study of As-Cast and dealloyed (foam) sample were carried out.

4.2 Characterization:

4.2.1 Characterization of as-cast and developed high entropy foams:

Crystal structure characterization (XRD Analysis):

With the help of XRD measurements, crystal structure characterizations of the as-cast (S1-S5) and dealloyed (FS2-FS5) samples were carried out. XRD results are displayed in fig.24. XRD graph of base NbTiVZr HEA (S1) shows the presence of only BCC (beta) phase. By adding yttrium, hcp phase at $2\theta = 28^{\circ}$, 31°, 32°, 50° and 60° has evolved. Relative intensity of the peaks corresponding to yttrium (hcp) became more significant as its concentration increases from S2 (5 At. %) to S5 (15 At. %). As-Cast samples S2-S5 show 2 phases, one beta (BCC) phase and one hcp phase evolved because of yttrium addition. XRD patterns of dealloyed samples only show BCC phase. No peaks corresponding to hcp phase were present in dealloyed (FS2-FS5) samples; thereby confirming complete removal of yttrium from interdendritic regions. XRD analysis results indicate the successful development of NbTiVZr high entropy foams (FS2-FS4).

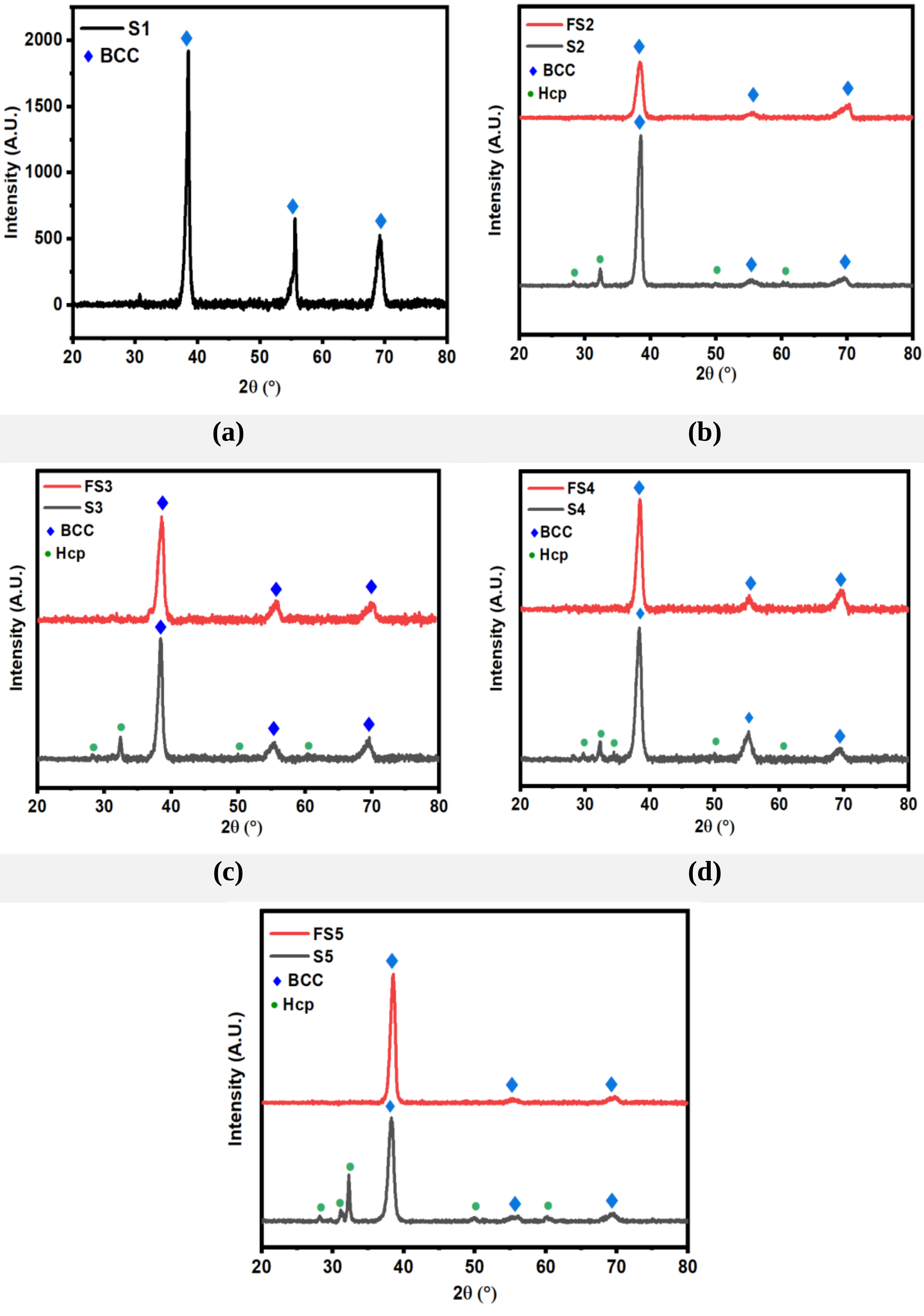

(a)

(b)

(c)

(d)

(e)

Figure 24: XRD patterns of (a) S1, (b) S2 and FS2, (c) S3 and FS3, (d) S4 and FS4, (e) S5 and FS5.

4.2.2 Microstructural Characterization:

Scanning Electron Microscopy:

SEM and EDS analysis were used for the microstructural investigation of developed alloys. SEM images of the as-cast S2, as-cast S3, as-cast S4, and as-cast S5 are shown in Fig 3.

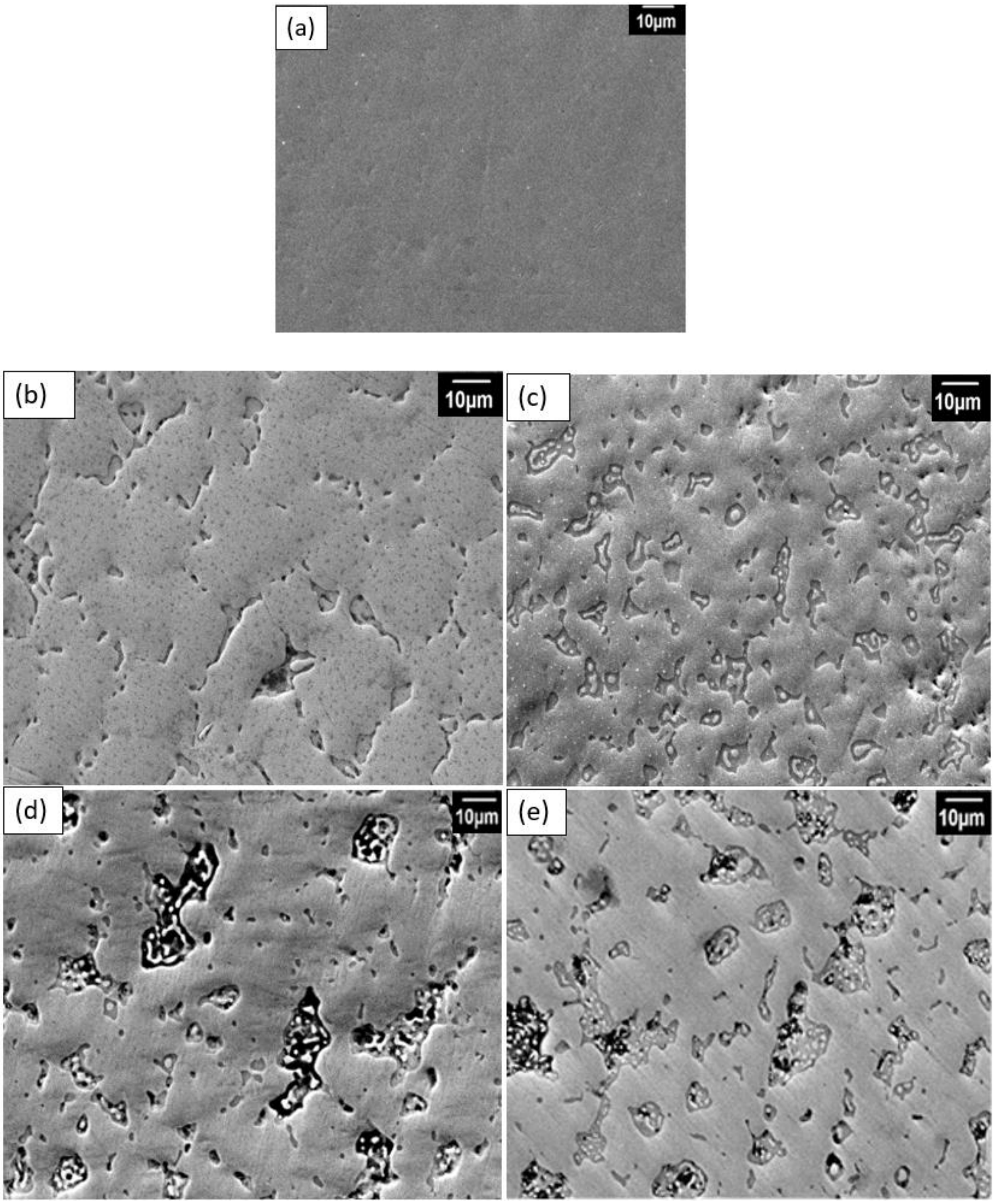

Figure 25: SEM images of (a) as-cast S1, (b) as-cast S2, (c) as-cast S3, and (d) as-cast S4, (e) as-cast S5.

The microstructure of S1 illustrates a single smooth solid grey region as shown in Fig. 25(a) which is classified as bcc phase from the XRD results shown in Fig. 24 (a).

Whereas the as-Cast high entropy alloys (S2-S5) showed two-phase contrast (light grey and dark grey) regions as shown in Fig.25 (b-e). Elemental distribution in these three phases was studied by elemental mapping, as seen in Fig. 26. Niobium, titanium, and vanadium were found to be uniformly distributed in the matrix (light grey region). Zirconium was found to be concentrated more in the interdendritic region along with yttrium. Yttrium was solely concentrated in the interdendritic (dark grey) regions as depicted by Fig.26 confirming its segregation.

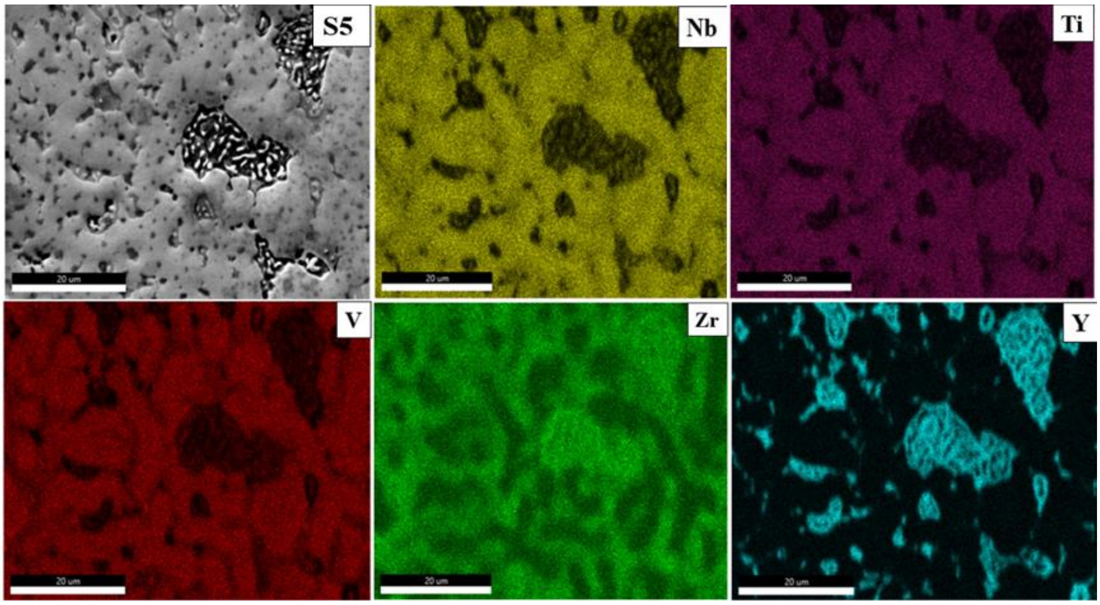

Figure 26: EDS mapping of as-cast S5 HEA.

3D porous structures can be developed by successful dissolution of yttrium from the interdendritic regions of as-cast S2-S5 samples. Nitric acid was used as chemical etchant for as it can preferentially dissolve yttrium from the interdendritic regions during dealloying process. Samples were weighed before and after dealloying and weight loss was recorded. Foams of S2, S3, S4 and S5 compositions, obtained after electrochemical dealloying, were named FS2, FS3, FS4 and FS5 respectively. SEM and EDS analysis were again carried out to study the effect of electrochemical dealloying in FS2-FS5 foams and are shown in Fig. 27 and Fig. 28 respectively.

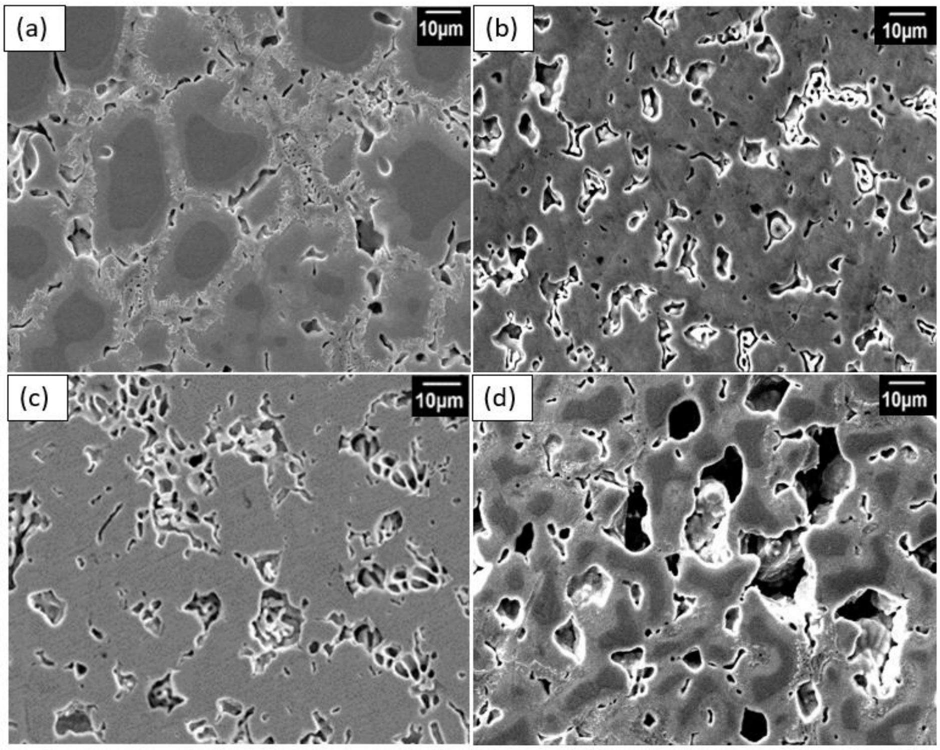

Figure 27: SEM images of (a) FS2, (b) FS3, (c) FS3, and (d) FS5.

After the dealloying process, SEM images show only light grey region (BCC phase, matrix) as shown in Fig. 27. EDX elemental mapping was used to analyze the distribution of elements after dealloying process, and results are shown in fig 28. Elemental mapping confirms the uniform distribution of Nb, Ti, V, and Zr throughout the light grey matrix. Whereas yttrium was found to be completely removed from interdendritic regions confirming the formation of porous network. Both SEM and EDS mapping confirms the formation of porous structure in HEA resulting from the removal of yttrium from interdendritic regions.

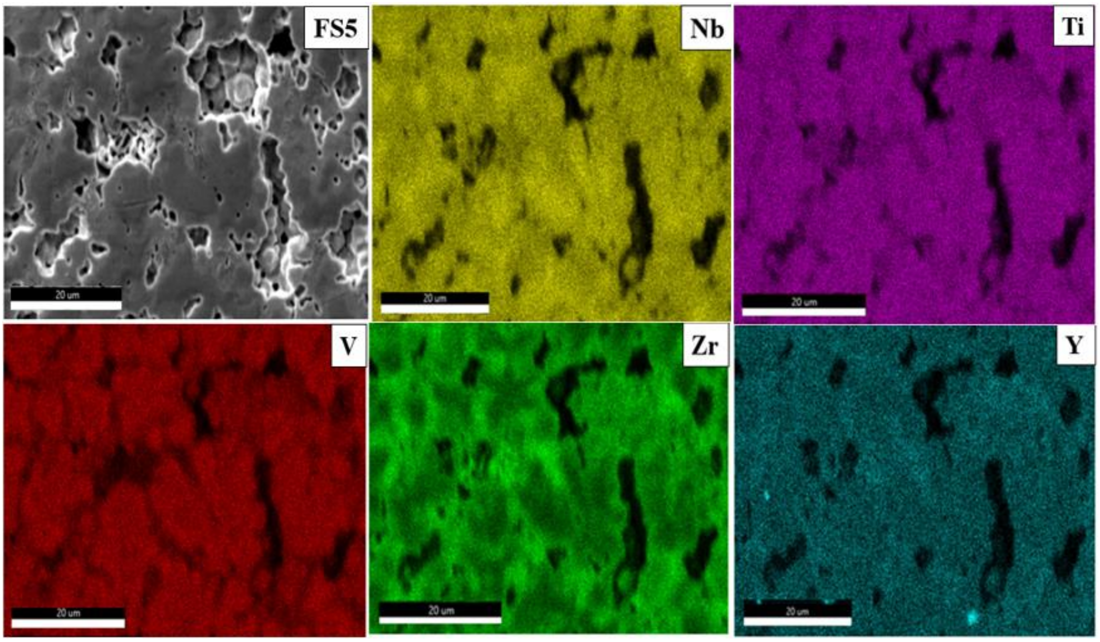

Figure 28: Elemental map analysis of as-Cast S5 and dealloyed FS5 sample.

4.3 Gravimetric analysis:

To confirm the removal of the filler element and the creation of high entropy foams, gravimetric studies were carried out. As cast samples (S2-S5) were immersed in an aqueous nitric acid solution for 24 hours, high entropy foams (FS2-FS5) were produced as the filler element was removed during the dealloying process. The weight of the alloys was measured before and after the dealloying process. Weight loss resulting from the removal of filler elements was presented as a function of the filler element is shown in fig.29 The amount of filler element added to the as-cast alloys causes a proportionate rise in weight loss.

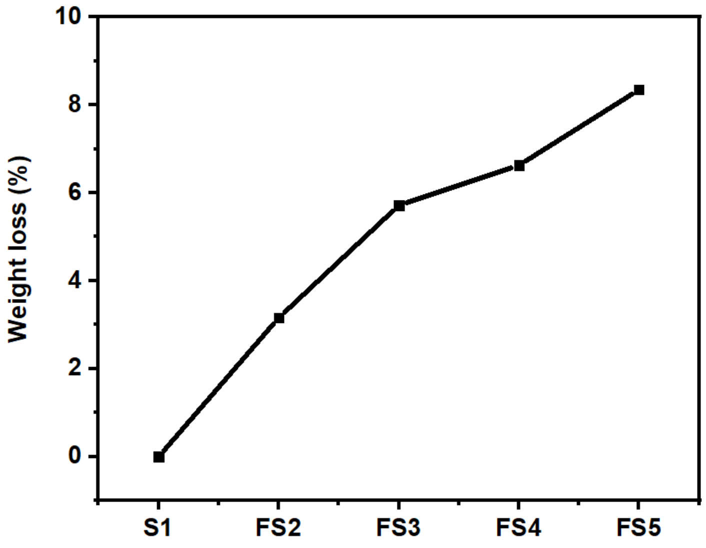

Figure 29: weight loss in dealloying process.

4.4 Electrochemical Characterization:

For electrochemical testing of developed samples electrolyte was optimized. Acidic (H_2SO_4), and alkaline (KOH) electrolytes exhibit higher ionic conductivity [70]. Alkaline and acidic electrolytes have a high corrosiveness, which is one of its drawbacks. Due to their corrosive nature, the electrode material may peel away from the substrate surface; this can be remedied by utilizing neutral electrolyte (e.g., Li_2SO_4, Na_2SO_4) [71]. Although, neutral electrolytes show lower ionic conductivities, they exhibit large working potential windows, less corrosion, environmental friendliness, and greater safety [72].

Also, in aqueous electrolytes (H_2SO_4, KOH, Na_2SO_4, Li_2SO_4), maximum working potential window is decided by water decomposition limit ~ 1.23V (evolution of H_2/O_2 at 1 atm pressure, at room temperature). However, there are reports showing the possibility to exceed limit using different configurations and particular type of aqueous electrolyte [73].

FS5 was used as test sample and while keeping in mind merits and demerits, electrochemical testing was performed in 1M aqueous solution of KOH, H_2SO_4, and Na_2SO_4 respectively. Cyclic voltammetry of FS5 was performed in 1M KOH in various potential windows [fig 30 (a)]. However, sample was only stable in negative (anodic) region i.e -1 to 0V ($\Delta V=1V$). Gases start to evolve at counter electrode (platinum wire) above 0 volts making is impossible to perform in the positive voltage range. Afterwards, the sample FS5 was tested in 1M H_2SO_4 electrolyte [fig.30 (b)]. It was somewhat stable in -0.5 to 0.5V potential window with small area under the curve. However, before and after -0.5V and 0.5V there was sharp rise in reduction and oxidation currents respectively. These findings indicate the inability of FS5 to perform in wide potential range in case of alkaline and acidic electrolytes. Also, the absence of redox peaks suggests that charge storage is only caused by the formation of an electrochemical double layer in a KOH and H_2SO_4 solution.

Final testing was performed in 1M Na_2SO_4 aqueous solution in various of potential ranges of -1 to +1V (ΔV=2V), 0.7 to 0.7V (ΔV=1.4V), -0.5 to 0.5V (ΔV=1V), -1 to 0V (ΔV=1V), 0 to 1V (ΔV=1V), -0.6 to 0.2V (ΔV=0.8V), and -0.2 to 0.6V (ΔV=0.8V) respectively [CV graph in Fig 30 (c)]. Current response in case of -1 to +1V (ΔV=2V) is higher as compared to rest of potential ranges. In this region not only the area under the curve is significant but also oxidation (0.25V) and reduction peaks (0.0V) are more significant in case of -1 to +1V. This implies that in large potential windows, intercalation/deintercalation activities or reversible redox reactions are more advantageous, while low current response in smaller potential windows may be caused by double layer contribution. With neutral electrolyte i.e Na_2SO_4, extended potential window can be stabilized [71].

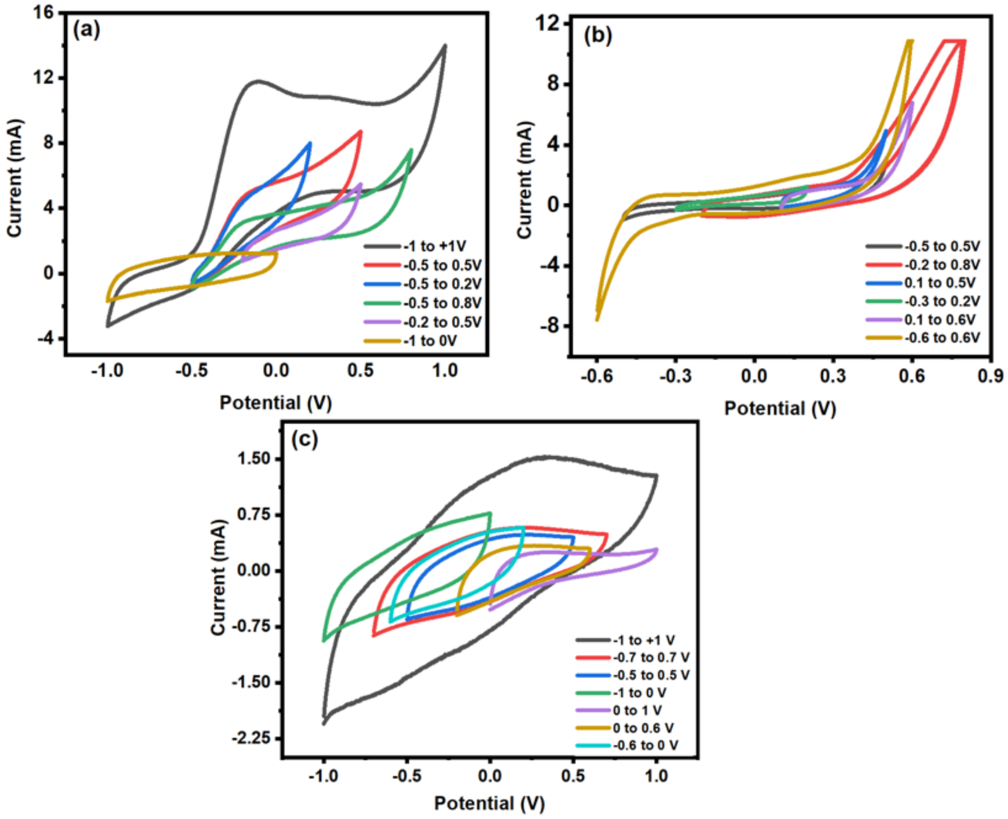

Figure 30: CV analysis of FS5 in 1M aqueous solution of (a) KOH, (b) H_2SO_4, and (c) Na_2SO_4, in various potential windows.

The reason for getting extended potential window is following: (a) The H^+| OH^- equilibrium produced by the neutral aqueous electrolyte Na_2SO_4 assures that electrodes are not accessible to both OH^- anions and H^+ (i.e., H_3O^+) for O_2 and H_2 evolution. (b) Moreover, due to highly solvated cations and sulphate anions, decomposition potential of electrolyte is larger than the water's thermodynamic decomposition potential (1.23 V) [74].

Thus, 1M Na_2SO_4 was chosen as electrolyte and three electrode setup is used for electrochemical measurements of all the samples (S1-FS5) in extended voltage range of -1 to +1V (ΔV=2V).

In a three-electrode measurement setup, the electrochemical testing of generated HEA foams (FS2-FS5) was conducted in comparison to the base S1 (NbTiVZr) sample using 1M Na_2SO_4 as an aqueous electrolyte, Ag/Agcl is used as reference electrode while platinum wire is used as counter electrodes. Cyclic voltammetry was carried out in the voltage range of -1 to +1 at various scan rates of 10, 20, 30, 50, 80, and 100 mVs^{-1}, and the results are shown in Fig. 31 to help explain the charge storage behaviour of the samples.

All the samples exhibit quasi-rectangular characteristics. At 0.25 V samples showed oxidation peaks while at 0.0 V all the samples showed reduction peak, indicating that all of the samples' active metal centres go through sequential redox reactions throughout the voltage range. This may be due to the cumulative effect of charge adsorption on the sample surface and cation (H^+ and Na^+) intercalation/deintercalation within the active porous structure. [2]. The lack of distinct redox peaks and quasi-rectangular features supports that charge storage was either caused by the cation's rapid surface adsorption/desorption process or by intercalation/deintercalation in the base S1 sample and developed FS2- FS5 foams. According to the equation given below [75] and shown in Fig. 31, the samples' areal capacitance (Ca) was determined from their CV curves.

$$Ca = \frac{I\ (V)dV}{Av\ (V_2 - V_1)}$$

Here, the potential window is (V_2 -V_1), v the scan rate is (V s^{-1}), and the working electrode area is A (cm^2). Table 4 compares the calculated areal capacitance values for all samples at various scan rates (2 mV/sec to 100 mV/sec). The base sample HEA sample (S1) has a capacitance of 1.96 mF/cm2 (2 mV/sec). The capacitance values for FS2, FS3, FS4 and FS5 are 4.82, 5.7%, 7.70, 34.54 and 82.66 mF/cm^2 respectively at 2mV/sec. It is evident from the results that porous foams (FS2-FS5) show a higher capacitance and enveloped the larger area under the curve (Fig. 31) than the S1 nonporous sample. Porous samples have directed channels (Fig. 27) and high surface area resulting in more intense peaks (Fig.31) and higher capacitance than S1. Comparison of current response from CV graphs in S1 and FS2-FS5 samples is an indication of ionic conductivity enhancement with the increase in porosity.

Table 4 shows that all the samples' capacitance values decrease as scan rates increase. This is because charge carriers' diffusion is limited at higher scan rates, as can be observed [76], [77]. The electrode's response current increases as the scan rate increases, which determines the electrode's superb kinetics and reversibility [19]. Figure 31 illustrates that even at 100 mV s^{-1}, the redox peaks are still present, which demonstrates the material's high-rate capacity. The value obtained for sample FS5

(82.66 mF/cm^2 at 2 mV/sec) is significantly greater than the earlier reported values of mono and binary refractory metal oxides and nitrides (Fig. 32a) calculated from the CV curves (15–35 mF cm^2) under similar scan rates [5], [56], [23], [55]. E.g on silicon substrate A. Achour and co-authors deposited Titanium vanadium nitride (TiVN) films. Using 1 M KOH as active electrolyte, and at a scan rate of 2 mVs^{-1}, around 15 mF/cm^2 capacitance value is achieved with 1:1 Ti/V in the film. At the sacn rate of 2 mV/sec, using 1 M KOH aqueous solution as the active electrolyte, this group noticed an increase in the Ca-value up to 24 mFcm^{-2}, with Ti/V ratio in film close 0.7 [5] to which is nonetheless less than the current report. For instance, at 2 mV/sec, areal capacitance of FS5 is also higher than that of Titanium nitride (TiN) films (12 mF/cm^2) [27], and TiN film (8.2 mF cm$^{−2}$) [23]. In addition, it is similar to those of TiO_2/Nb_2O_5 nitrided nanotubes electrodes (35 mF/cm^2 at 1 mV/sec) [55]. Fig. 33 displays a comparison with numerous other metal nitrides and metal oxides.

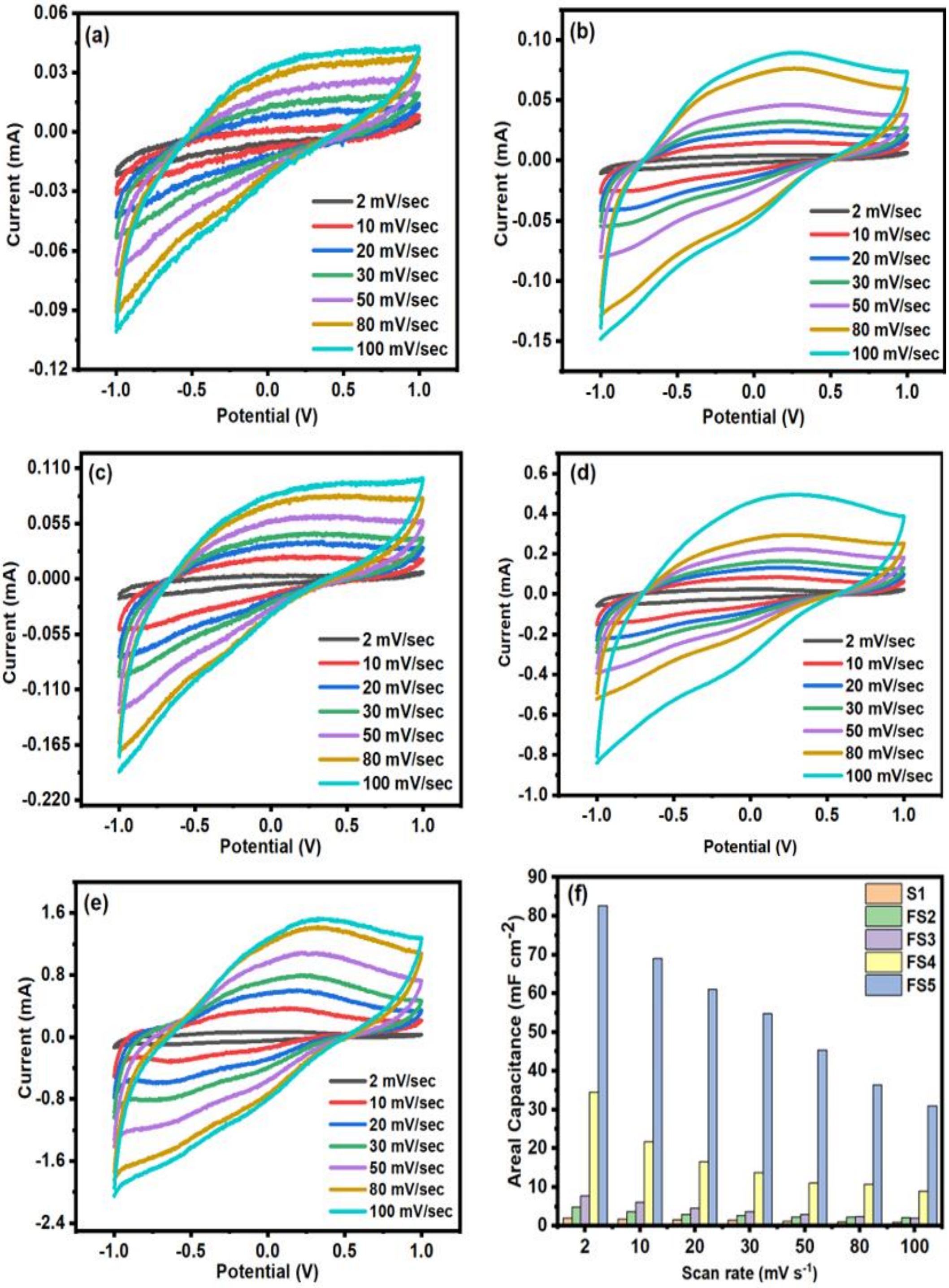

Figure 31: Cyclic voltammograms of (a) as-cast S1 (b) FS2 (c) FS3 (d) FS4 (e) FS5 and (f) Comparison of the capacitance values of all the S1-FS5 samples as a function of scan rates, calculated from the CV data.

Table 4: Values of areal capacitance (Ca) for all the samples calculated from CV data.

Scan Rate (mV/sec)	**Capacitance (mF/cm^2)**				
	S1	**FS2**	**FS3**	**FS4**	**FS5**
2	1.96	4.82	7.70	34.54	82.66
10	1.76	3.66	6.06	21.73	69.06
20	1.65	2.97	4.52	16.53	61.04
30	1.47	2.61	3.70	13.70	54.78
50	1.20	2.22	2.94	11.05	45.44
80	0.98	2.22	2.33	10.76	36.40
100	0.90	2.12	2.05	8.99	31.03

The galvanostatic charge-discharge analysis on FS2-FS5 foams against the base S1 sample was performed to assess the charge discharge behaviour, rate capability, and capacitance of all the samples. In Fig. 32, over the same potential window (-1 to +1), GCD curves for each sample are displayed with the same 3 electrode electrochemical setup as used in CV measurements, at 100, 300, 500, 700, 900 and 1000 $\mu A\ cm^{-2}$ current densities. The areal capacitances (Ca) of the samples are calculated from the GCD curves according to the following equation [75].

$$Ca = \frac{I\Delta t}{\Delta VA}$$

Thus, I (A) denotes the discharge current, Δt (s) the discharge duration, ΔV (V) the potential change resulting from the discharge, and A (cm^2) the working electrode's surface area. Table 5 compares corresponding Ca-values for all samples at current densities of 100, 300, 500 and 700, $\mu A/cm^2$. Base S1 sample (NbTiVZr) shows the capacitance value of 0.74 mF/cm^2 (100 $\mu A/cm^2$). Whereas porous samples FS2, FS3, FS4 and FS5 shows the capacitance values of 1.05, 7.23, 29.85, and 71.29 mF/cm^2 at 100 $\mu A/cm^2$ as calculated from GCD data. The fact that porous samples offer higher active surface sites for better utilization of the active material accounts for the increased capacitance values in FS2-FS5 foams compared to the base S1 sample [19].

As the value of current density increases the value of capacitance decreases. The main causes of this are that the active ingredient utilization rate decreases at high current densities. [78]. The potential-time curves are seen to be relatively symmetrical. The redox peaks in CV curves are consistent with the unique potential plateaus that each curve has at 0.0V (Fig. 31) [79]. Deviations from the linear behaviour in GCD profiles of all the electrodes, reveals that the charge storage mechanisms are due to both faradic pseudocapacitive reaction [80] and charge adsorption on sample surface.

The FS5 sample performed the best when compared to the other samples in GCD results as well as CV in term of capacitance values, suggesting that electrode performance is highly reproduceable and consistent in both situations. The greatest Ca value found for sample FS5 is 71.29 mF cm2, which is significantly higher than the mono- and binary-MO and metal nitrides values previously published and computed from the GCD curves as shown in Fig. 33.

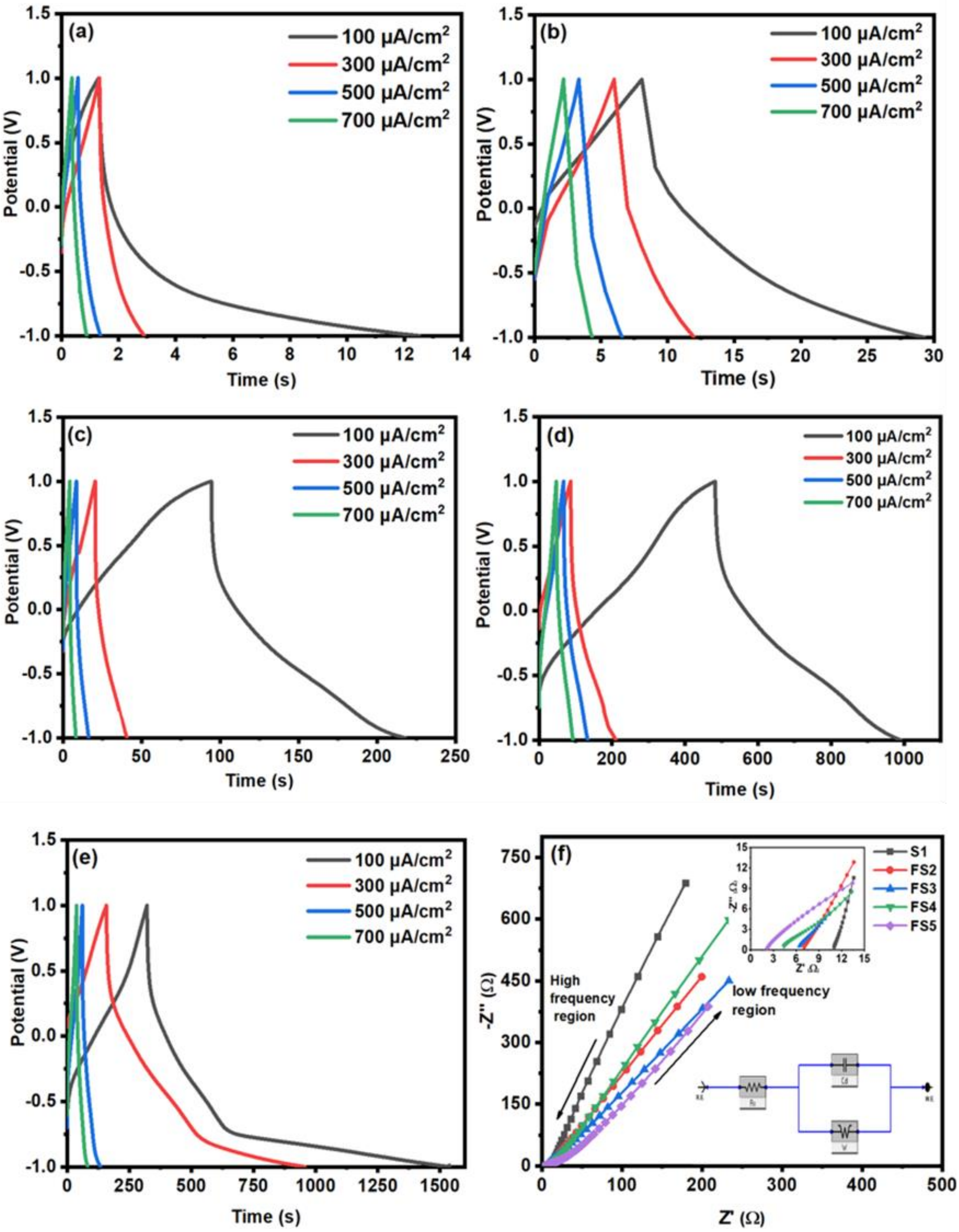

Figure 32: Galvanostatic charge-discharge curves of (a) as-cast S1, (b) FS2, (c) FS3, (d) FS4, and (e) FS5 at various current densities (f) Nyquist plots of as-cast S1- FS5 samples.

EIS measurements are carried out for FS2-FS5 foams against the S1 sample to comprehend the kinetic properties. Figure 32 (f) shows the Nyquist plot of all samples from low to high frequency regions, while inset of figure 32 (f) shows the plot for mid- to high-frequency regions. Each plot contains a linear part in the high- and low-frequency regions. Absence of semicircular region in the high frequency area [fig 32

(f) inset] demonstrates that all the samples have negligible charge transfer resistance (Rct). Also, the high frequency intercept on the real axis (Z') reflects the series resistance (R), is the contact resistance at the solid-liquid interface, internal resistance of the active material and the electrolyte (ionic) resistance [81].

Considering the shape of Nyquist plot shown in Fig 32 (f), the EIS data are fitted with equivalent circuit as shown in the figure’s inset [82], [83]. Samples S1, FS2, FS3, FS4 and FS5 showed the Rs (series resistance) values of 11.01Ω, 7.03Ω, 6.41Ω, 4.37Ω and 2.19Ω respectively. Rs value of the base S1 sample is higher than the porous samples indicating that porosity play significant role in decrease of resistance. The Rs results show that when porosity increases from FS2-FS5, the internal resistance and the contact resistance at the solid-liquid interface decrease, enhancing ionic conductivity and rate capability for superior supercapacitor applications. The FS5 sample displayed larger areal capacitances compared to other samples, demonstrating robust and highly reproducible electrochemical characteristics of the samples. The fitted EIS data is also comparable with the CV and GCD data 1(Figs 31, 32, and Table 4). The FS5 sample's superior electrochemical properties over those of other samples have already been discussed in the preceding section, and they are mostly attributable to its adequate porosity, which results in more active sites and, thus, better utilization of active material.

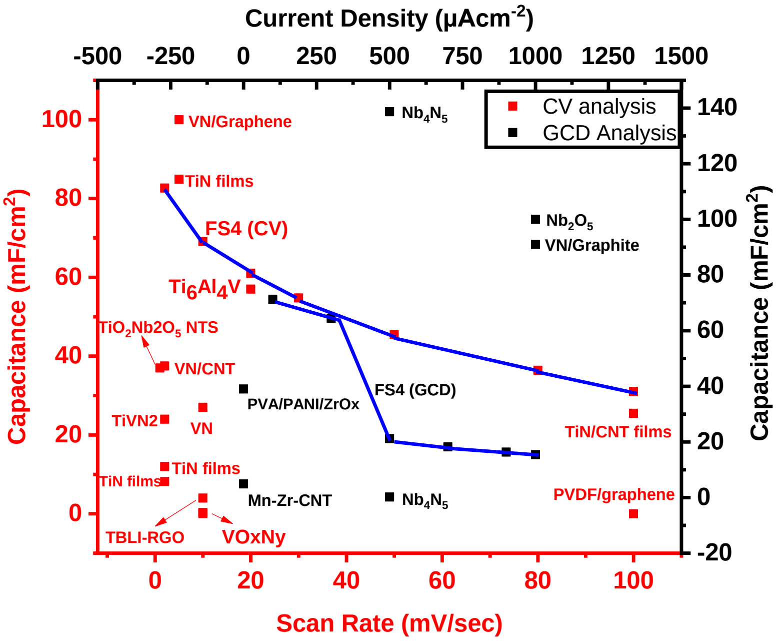

Figure 33: Comparison of FS4 areal capacitance with literature values calculated from the
CV and GCD curves [2, 5], [23, 47-49], [51-56], [84-88].

A long cycling life with excellent capacity retention is a key aspect for improved electrochemical performance in supercapacitor applications. The capacity retention graphs of the FS5 sample for nearly 5000 cycles at a current density of 1 mA cm^{-2} (1000 μA/cm^{2}) are displayed in Figure 34(a). After 5000 cycles, the FS5 sample retains 104% of its initial capacitance value, demonstrating its high stability. This could be attributed to HEA's high structural stability, which precludes electrode expansion and contraction [11]. The coulombic efficiency of 96.35% is also displayed by electrode.

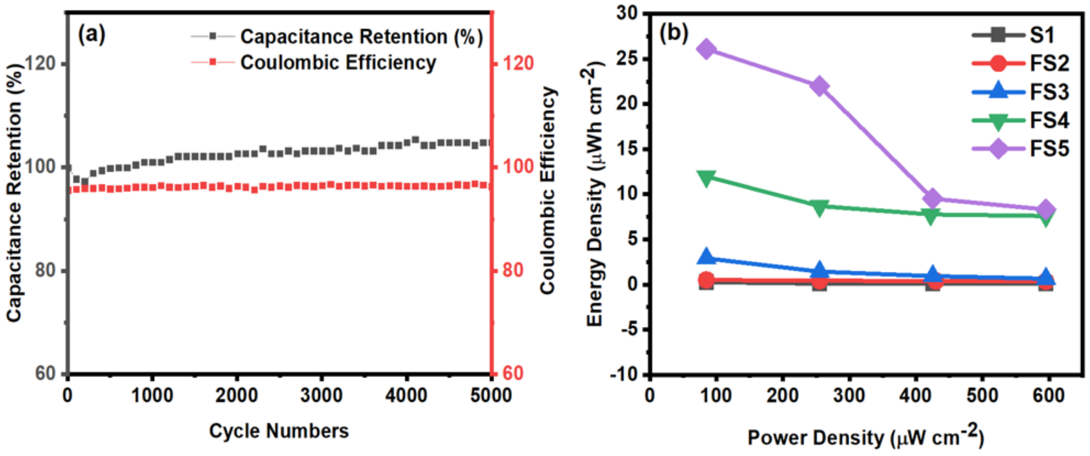

Figure 34: Cyclic stability of FS5 sample at current density of 1 mA cm^{-2} (b) Ragone plots of power density versus energy density for all the samples.

The Ragone plot of areal energy density (mWh cm^2) vs power density P (mW cm^2), which was obtained using the equations given below using the GCD curves, is used to analyze the corresponding energy and power density of the porous (FS2-FS5) electrodes. [39]:

$$\boldsymbol{E.d} = \frac{\mathbf{1}}{\mathbf{2}}\mathbf{CV^2}$$

$$\boldsymbol{P.d} = \frac{\boldsymbol{E.d}}{\boldsymbol{\Delta t}}$$

and Δt, in sec is the discharge time. It's important to note that, even though Ragone plots are typically used for packaged devices rather than an electrochemical electrode (half-cell), but it is appropriate to isolate the energy and power density of individual half-cell components (like electrolyte or electrode) with the advent of new electrode material in order to understand the effect of these components on the overall electrochemical performance while avoiding the cost of manufacturing a packaged device [89].

To illustrate the exceptional energy and power behaviour of these electrodes synthesized in 1 M Na_2SO_4 solution, Ragone plots for FS2-FS5 electrodes are provided in Fig. 34 (b). Inferring extraordinarily stable and repeatable electrochemical performance of the HEA electrodes, this is obviously congruent with the CV, GCD results.

The two following reasons are primarily responsible for the current samples' improved electrochemical characteristics in comparison to previously reported values: (1) new manufacturing method employed, in which because of the porous network of samples, the electrons transmission path is much shorter [18]. Also, porous samples provide increased use of the active substance through increased active surface sites; [19] thus, the results show that the dealloyed HEA porous electrode can charge/ discharge faster and more efficiently [18]. (2) Because more Faradaic redox processes take place at the interface of the electrocapacitive material and the electrolyte in case of HEA, so when compared with single and binary metal nitrides and oxides they exhibit greater electrochemical behaviour. Considering this idea, it would be interesting to find out if adding more transition metals to the electrocapacitive material will result in a greater number of Faradaic redox processes and higher specific capacitances. By including more metals in the metal oxides, it was possible to improve ionic conductivity and reduce resistance in addition to the capacitance enhancement because of more Faradaic redox involved [90].

4.5 Conclusion:

1. NiTiVZrY foams have been successfully developed by the insertion of yttrium in the base HEA and its removal by electrochemical dealloying process.
2. Developed NiTiVZrY foams displayed excellent electrochemical properties. Among all the developed foams, FS5 exhibited the highest areal capacitance value of 85mF cm^{-2} at the scan rate of 2mV s^{-1}.
3. FS5 electrode demonstrated high cyclic stability and displayed capacitance retention of 104% after 5000 cycles at 1 mA cm^{-2} current density.
4. The outstanding electrochemical properties of developed foams is due to higher surface adsorption sites in the samples and porous network which facilitates higher ion diffusion and improves electrochemical interactions resulting in lower ESR values.

4.6 Future Work:

S1 and FS2-FS5 foams can perform in large voltage range. High energy densities are possible with a wide potential window because they are directly proportional to the square of operating potential. Subsequently, the prepared samples (S1-FS5) are suitable candidates for integration in devices [71].

References

[1] Naeem Ashiq, M., et al., *Enhanced electrochemical properties of silver-coated zirconia nanoparticles for supercapacitor application.* (2021). **15**(1): p. 10-16.

[2] Upadhyay, K.K., et al., *Capacitance response in an aqueous electrolyte of Nb2O5 nanochannel layers anodically grown in pure molten o-H3PO4.* (2018). **281**: p. 725-737.

[3] Iro, Z.S., C. Subramani, and S.J.I.J.E.S. Dash, *A brief review on electrode materials for supercapacitor.* (2016). **11**(12): p. 10628-10643.

[4] González, A., et al., *Review on supercapacitors: Technologies and materials.* (2016). **58**: p. 1189-1206.

[5] Achour, A., et al., *Titanium vanadium nitride electrode for micro-supercapacitors.* (2017). **77**: p. 40-43.

[6] Kong, K., et al., *Nanoporous structure synthesized by selective phase dissolution of AlCoCrFeNi high entropy alloy and its electrochemical properties as supercapacitor electrode.* (2019). **437**: p. 226927.

[7] Chandra, A.J.P.o.t.N.A.o.S., India Section A: Physical Sciences, *Supercapacitors: an alternate technology for energy storage.* (2012). **82**(1): p. 79-90.

[8] Mao, A., et al., *A new class of spinel high-entropy oxides with controllable magnetic properties.* (2020). **497**: p. 165884.

[9] Miller, E.E., Y. Hua, and F.H.J.J.o.E.S. Tezel, *Materials for energy storage: Review of electrode materials and methods of increasing capacitance for supercapacitors.* (2018). **20**: p. 30-40.

[10]. Vangari, M., T. Pryor, and L.J.J.O.E.E. Jiang, *Supercapacitors: Review of Materials.* (2013). **2**: p. 72-79.

[11] Zhou, H. and J.J.F.i.E.R. He, *Synthesis of the New High Entropy Alloy and Its Application in Energy Conversion and Storage.* (2020). **8**: p. 73.

[12] Shown, I., et al., *Conducting polymer-based flexible supercapacitor.* (2015). **3**(1): p. 2-26.

[13] Beidaghi, M., W. Chen, and C. Wang. *Design, fabrication, and evaluation of on-chip micro-supercapacitors*. in *Energy Harvesting and Storage: Materials, Devices, and Applications Ii*. (2011). SPIE.

[14] Zhao, T., et al., *In situ synthesis of interlinked three-dimensional graphene foam/polyaniline nanorod supercapacitor.* (2017). **230**: p. 342-349.

[15] Inagaki, M., H. Konno, and O.J.J.o.p.s. Tanaike, *Carbon materials for electrochemical capacitors.* (2010). **195**(24): p. 7880-7903.

[16] Park, N., et al., *Recrystallization behavior of CoCrCuFeNi high-entropy alloy.* (2015). **46**(4): p. 1481-1487.

[17] Basu, R., et al., *Phase-pure VO2 nanoporous structure for binder-free supercapacitor performances.* (2019). **9**(1): p. 1-11.

[18] Chen, P.-C., et al., *Selectively dealloyed Ti/TiO2 network nanostructures for supercapacitor application.* (2014). **133**: p. 175-178.

[19] Banerjee, A.N., V. Anitha, and S.W.J.S.r. Joo, *Improved electrochemical properties of morphology-controlled titania/titanate nanostructures prepared by in-situ hydrothermal surface modification of self-source Ti substrate for high-performance supercapacitors.* (2017). **7**(1): p. 1-20.

[20] Wei, F., et al., *3D N, O-codoped egg-box-like carbons with tuned channels for high areal capacitance supercapacitors.* (2020). **12**(1): p. 1-12.

[21] Yu, Z., et al., *Supercapacitor electrode materials: nanostructures from 0 to 3 dimensions.* (2015). **8**(3): p. 702-730.

[22] Qiao, D.-X., et al., *A novel series of refractory high-entropy alloys Ti2ZrHf0. 5VNbx with high specific yield strength and good ductility.* (2019). **32**(8): p. 925-931.

[23] Achour, A., et al., *Role of nitrogen doping at the surface of titanium nitride thin films towards capacitive charge storage enhancement.* (2017). **359**: p. 349-354.

[24] Tai, M.C.Q., *Production of optically functional nanoscale structures by chemical de-alloying of metallic precursor alloys*. (2019).

[25] Cantor, B., et al., *Microstructural development in equiatomic multicomponent alloys.* (2004). **375**: p. 213-218.

[26] Yeh, J.W., et al., *Nanostructured high-entropy alloys with multiple principal elements: novel alloy design concepts and outcomes.* (2004). **6**(5): p. 299-303.

[27] Tsai, M.-H. and J.-W.J.M.R.L. Yeh, *High-entropy alloys: a critical review.* (2014). **2**(3): p. 107-123.

[28] Gaskell, D.R. and D.E. Laughlin, *Introduction to the Thermodynamics of Materials*. (2017): CRC press.

[29] Lucas, M., et al., *Absence of long-range chemical ordering in equimolar FeCoCrNi.* (2012). **100**(25): p. 251907.

[30] Tsai, M.-H.J.E., *Physical properties of high entropy alloys.* (2013). **15**(12): p. 5338-5345.

[31] Cheng, K.-H., et al. *Recent progress in multi-element alloy and nitride coatings sputtered from high-entropy alloy targets*. in *Annales de chimie (Paris. 1914)*. (2006).

[32] Tsai, K.-Y., M.-H. Tsai, and J.-W.J.A.M. Yeh, *Sluggish diffusion in co–cr–fe–mn–ni high-entropy alloys.* (2013). **61**(13): p. 4887-4897.

[33] Chen, Y., et al., *Corrosion properties of a novel bulk Cu0. 5NiAlCoCrFeSi glassy alloy in 288° C high-purity water.* (2007). **61**(13): p. 2692-2696.

[34] Singh, S., et al., *Decomposition in multi-component AlCoCrCuFeNi high-entropy alloy.* (2011). **59**(1): p. 182-190.

[35] Tsai, M.-H., et al., *Thermal stability and performance of NbSiTaTiZr high-entropy alloy barrier for copper metallization.* (2011). **158**(11): p. H1161.

[36] Mei, J., et al., *Cobalt oxide-based nanoarchitectures for electrochemical energy applications.* (2019). **103**: p. 596-677.

[37] Vickers, N.J.J.C.b., *Animal communication: when i'm calling you, will you answer too?* (2017). **27**(14): p. R713-R715.

[38] Zhang, Y., et al., *Robust production of ultrahigh surface area carbon sheets for energy storage.* (2018). **14**(19): p. 1800133.

[39] Liu, Y., et al., *A template-catalyzed in situ polymerization and co-assembly strategy for rich nitrogen-doped mesoporous carbon.* (2018). **6**(7): p. 3162-3170.

[40] Meng, Q., et al., *Research progress on conducting polymer based supercapacitor electrode materials.* (2017). **36**: p. 268-285.

[41] Snook, G.A., P. Kao, and A.S.J.J.o.p.s. Best, *Conducting-polymer-based supercapacitor devices and electrodes.* (2011). **196**(1): p. 1-12.

[42] Ersozoglu, M.G., et al., *A novel dioxythiophene based conducting polymer as electrode material for supercapacitor application.* (2019). **14**: p. 9504-9519.

[43] Ates, M., A.J.P.-P.T. Dolapdere, and Engineering, *Poly (3-octylthiophene) and poly (3-octylthiophene)/TiO2-coated on Al1050: electrosynthesis, characterization and its corrosion protection ability in NaCl solution.* (2014). **53**(17): p. 1768-1777.

[44] Laforgue, A., et al., *Activated carbon/conducting polymer hybrid supercapacitors.* (2003). **150**(5): p. A645.

[45] Xu, J., et al., *Preparing two-dimensional microporous carbon from Pistachio nutshell with high areal capacitance as supercapacitor materials.* (2014). **4**(1): p. 1-6.

[46] Zhou, J., et al., *Nitrogen Codoped Unique Carbon with 0.4 nm Ultra-Micropores for Ultrahigh Areal Capacitance Supercapacitors.* (2018). **14**(36): p. 1801897.

[47] Wang, Y.S., et al., *Toward Metal–Organic-Framework-Based Supercapacitors: Room-Temperature Synthesis of Electrically Conducting MOF-Based Nanocomposites Decorated with Redox-Active Manganese.* (2019). **2019**(26): p. 3036-3044.

[48] Fu, X.-Y., et al., *Free-standing and flexible graphene supercapacitors of high areal capacitance fabricated by laser holography reduction of graphene oxide.* (2021). **118**(7): p. 071601.

[49] Le, V.T., et al., *Simultaneous enhancement of specific capacitance and potential window of graphene-based electric double-layer capacitors using ferroelectric polymers.* (2021). **507**: p. 230268.

[50] Wu, X., et al., *Insight into high areal capacitances of low apparent surface area carbons derived from nitrogen-rich polymers.* (2015). **94**: p. 560-567.

[51] Myasoedova, T., et al., *Structure and Electrochemical Properties of PANI/ZrOX and PANI/SiOX Composites.* (2020). **49**(8): p. 4707-4713.

[52] Ouldhamadouche, N., et al., *Electrodes based on nano-tree-like vanadium nitride and carbon nanotubes for micro-supercapacitors.* (2018). **34**(6): p. 976-982.

[53] Durai, G., et al., *Influence of chromium content on microstructural and electrochemical supercapacitive properties of vanadium nitride thin films developed by reactive magnetron co-sputtering process.* (2019). **45**(10): p. 12643-12653.

[54] Porto, R.L., et al., *Titanium and vanadium oxynitride powders as pseudo-capacitive materials for electrochemical capacitors.* (2012). **82**: p. 257-262.

[55] Ozkan, S., et al., *Highly Conducting Spaced TiO $ _2 $ Nanotubes Enable Defined Conformal Coating with Nanocrystalline Nb $ _2 $ O $ _5 $ and High Performance Supercapacitor Applications.* (2020).

[56] Achour, A., et al., *Titanium nitride films for micro-supercapacitors: effect of surface chemistry and film morphology on the capacitance.* (2015). **300**: p. 525-532.

[57] Fu, M., et al., *High-entropy materials for energy-related applications.* (2021). **24**(3): p. 102177.

[58] Gludovatz, B., et al., *A fracture-resistant high-entropy alloy for cryogenic applications.* (2014). **345**(6201): p. 1153-1158.

[59] Rost, C.M., et al., *Entropy-stabilized oxides.* (2015). **6**(1): p. 1-8.

[60] Bérardan, D., et al., *Colossal dielectric constant in high entropy oxides.* (2016). **10**(4): p. 328-333.

[61] Meisenheimer, P., T. Kratofil, and J.J.S.r. Heron, *Giant enhancement of exchange coupling in entropy-stabilized oxide heterostructures.* (2017). **7**(1): p. 1-6.

[62] Zhai, S., et al., *The use of poly-cation oxides to lower the temperature of two-step thermochemical water splitting.* (2018). **11**(8): p. 2172-2178.

[63] Chen, H., et al., *Mechanochemical synthesis of high entropy oxide materials under ambient conditions: Dispersion of catalysts via entropy maximization.* (2019). **1**(1): p. 83-88.

[64] Wang, Q., et al., *High entropy oxides as anode material for Li-ion battery applications: A practical approach.* (2019). **100**: p. 121-125.

[65] Zhao, C., et al., *High-entropy layered oxide cathodes for sodium-ion batteries.* (2020). **59**(1): p. 264-269.

[66] Jin, T., et al., *Mechanochemical-assisted synthesis of high-entropy metal nitride via a soft urea strategy.* (2018). **30**(23): p. 1707512.

[67] Xu, X., et al., *High-entropy alloy nanoparticles on aligned electronspun carbon nanofibers for supercapacitors.* (2020). **822**: p. 153642.

[68] Kim, B.K., et al., *Handbook of clean energy systems.* (2015). **10**(1002): p. 9781118991978.

[69] Barsoukov, E. and J.R.J.A. Macdonald, 2nd ed., *Impedance Spectroscopy Theory, Experiment, and.* (2005).

[70] De, P., et al., *Role of porosity and diffusion coefficient in porous electrode used in supercapacitors–Correlating theoretical and experimental studies.* (2022): p. e2100159.

[71] Haldar, P.J.E.A., *Achieving wide potential window and high capacitance for supercapacitors using different metal oxides (viz.: ZrO2, WO3 and V2O5) and their PANI/graphene composites with Na2SO4 electrolyte.* (2021). **381**: p. 138221.

[72] Zhong, C., et al., *A review of electrolyte materials and compositions for electrochemical supercapacitors.* (2015). **44**(21): p. 7484-7539.

[73] Haldar, P., et al., *Mn3O4-polyaniline-graphene as distinctive composite for use in high-performance supercapacitors.* (2019). **491**: p. 171-179.

[74] Fic, K., et al., *Novel insight into neutral medium as electrolyte for high-voltage supercapacitors.* (2012). **5**(2): p. 5842-5850.

[75] Zhen, M., et al., *TiO 2–B nanorods on reduced graphene oxide as anode materials for Li ion batteries.* (2015). **51**(3): p. 507-510.

[76] Salari, M., et al., *Enhancement of the electrochemical capacitance of TiO 2 nanotube arrays through controlled phase transformation of anatase to rutile.* (2012). **14**(14): p. 4770-4779.

[77] Ke, Q., et al., *3D TiO2@ Ni (OH) 2 core-shell arrays with tunable nanostructure for hybrid supercapacitor application.* (2015). **5**(1): p. 1-11.

[78] Yang, W., et al., *Synthesis of vanadium oxide nanorods coated with carbon nanoshell for a high-performance supercapacitor.* (2020). **26**(2): p. 961-970.

[79] Zhang, Y. and Y.J.B.o.M.S. Huang, *Facile synthesis and characterization of rough surface $$\mathrm {V} _ {2}\hbox {O} _ {5} $$ V 2 O 5 nanomaterials for pseudo-supercapacitor electrode material with high capacitance.* (2017). **40**(6): p. 1137-1149.

[80] Li, S., et al., *In situ XPS studies of thermally deposited potassium on poly (p-phenylene vinylene) and its ring-substituted derivatives.* (2001). **181**(3-4): p. 201-210.

81. Wan, C., L. Yuan, and H.J.I.J.E.S. Shen, *Effects of electrode mass-loading on the electrochemical properties of porous MnO2 for electrochemical supercapacitor.* 2014. **9**(1).

82. Zhao, W., et al., *Enhanced photocatalytic activity for H2 evolution under irradiation of UV–Vis light by Au-modified nitrogen-doped TiO2.* 2014. **9**(8): p. e103671.

83. Wang, H., et al., *General and controllable synthesis strategy of metal oxide/TiO2 hierarchical heterostructures with improved lithium-ion battery performance.* 2012. **2**(1): p. 1-8.

84. Cui, H., et al., *Niobium nitride Nb4N5 as a new high-performance electrode material for supercapacitors.* 2015. **2**(12): p. 1500126.

85. Achour, A., et al., *Hierarchical nanocomposite electrodes based on titanium nitride and carbon nanotubes for micro-supercapacitors.* 2014. **7**: p. 104-113.

86. Ramadoss, A., et al., *Construction of light-weight and flexible vanadium nitride coated graphite paper electrodes for supercapacitors.* 2022. **28**(5): p. 2513-2524.

87. Zhao, C., et al., *Three dimensional (3D) printed electrodes for interdigitated supercapacitors.* 2014. **41**: p. 20-23.

88. Sun, N., et al., *Sputtered titanium nitride films with finely tailored surface activity and porosity for high performance on-chip micro-supercapacitors.* 2021. **489**: p. 229406.

89. Mai, L., et al., *Fast ionic diffusion-enabled nanoflake electrode by spontaneous electrochemical pre-intercalation for high-performance supercapacitor*. 2013. **3**(1): p. 1-8.

90. Huang, Y.-Y. and L.-Y.J.A.A.E.M. Lin, *Synthesis of ternary metal oxides for battery-supercapacitor hybrid devices: influences of metal species on redox reaction and electrical conductivity.* 2018. **1**(6): p. 2979-2990.